

# Optimal growth over a time-evolving variable-density jet at Atwood number $|At| = 0.25$

Gabriele Nastro<sup>1,†</sup>, Jérôme Fontane<sup>1</sup> and Laurent Joly<sup>1</sup>

<sup>1</sup>ISAE-SUPAERO, Université de Toulouse, France

(Received 29 June 2021; revised 23 November 2021; accepted 11 January 2022)

Secondary instabilities growing over a time-evolving variable-density round jet subject to the primary Kelvin–Helmholtz (KH) instability at Atwood number  $|At| = 0.25$  are investigated with a non-modal linear stability analysis. Despite local modifications of the base flow vorticity induced by the baroclinic torque, these disturbances experience a short-term universal growth due to a combination of the Orr and lift-up mechanisms, whatever the azimuthal wavenumber  $m$ . At  $Re = 1000$ , the secondary energy growth stems from the development of elliptical and hyperbolic instabilities, with an E-type-to-H-type transition as  $m$  and  $Re$  increase, as in the homogeneous case (Nastro *et al.*, *J. Fluid Mech.*, vol. 900, 2020, A13). In the light jet at  $Re = 1000$ , after the KH mode saturation, the high- $m$  H-type instability is replaced by a perturbation organised as counter-rotating streamwise vortices located in the base flow region of promoted strain rate. Increasing the Reynolds number up to  $Re = 10\,000$  yields larger energy growths and a strong anisotropy among energy and enstrophy components with a preferential increase of axial velocity and azimuthal vorticity. Both come from the linearised baroclinic source that drives the optimal response towards folded sheets of axial velocity that differ from those observed in the variable-density plane shear layers. When the perturbation is injected around the KH saturation time for  $Re = 10\,000$ , the response to optimal perturbation takes the form of fast growing secondary KH instabilities whatever  $m$ . We find these three-dimensional secondary KH instabilities to be good candidates for the transition to turbulence in variable-density jet flows.

**Key words:** jets

<sup>†</sup> Email address for correspondence: [nastrogabriele@gmail.com](mailto:nastrogabriele@gmail.com)

## 1. Introduction

Stability theory and transition in free shear flows have long been a subject of central importance in much research involving fluid mixing flow. Because of its frequent use in fluid engineering and its common occurrence in natural flows, the round jet is an archetypal open shear flow that has drawn a great deal of interest. The round jet transition is primarily governed by the development of co-rotating vortex ring structures associated with the Kelvin–Helmholtz (KH) instability of the cylindrical shear layer (Becker & Massaro 1968). This inviscid inflectional instability (Drazin & Reid 1981; Rayleigh 1892) can be properly characterised by a local linear modal stability analysis (Batchelor & Gill 1962; Lessen & Singh 1973; Crighton & Gaster 1976; Morris 1976; Plaschko 1979; Michalke 1984). The intensity and the spatial organisation of these primary vortex rings determine the dominant mechanism of the jet spreading through the entrainment of external quiescent fluid. This phenomenon, also defined as the ‘gulping’ of outer fluid triggered by the rolling-up of the axisymmetric jet shear layer, has been described by Dimotakis (1986) for the plane mixing layer. By extending his considerations from the shear layer to the round jet, three different stages can be distinguished in the evolution/spreading of a jet flow. The first phase called induction involves large-scale entrainment of external fluid pulled into the cylindrical shear layer as a result of the KH instability. There, a fluid element is deformed by the local strain field until its length scale is small enough to be smeared out by mass diffusion. This second stage is known as diastrophy and is also susceptible to hosting three-dimensional secondary instabilities. In the third stage, called infusion, the flow completes its transition to turbulence after a rapid development of small scales motions. The dynamics between the phases of induction and diastrophy is of crucial importance to understand the subsequent route to turbulence because the physical mechanisms involved in these stages trigger flow bifurcations and transition. To take a further step in this direction, we decompose the problem at stake into an unsteady base flow, developing a standard KH instability we call primary, and a perturbation that grows over the primary one which is therefore called secondary throughout this paper. Furthermore, when we refer to homogeneity here, we are referring only to density homogeneity.

In the homogeneous case, the stability analysis of Nastro, Fontane & Joly (2020) on the time-dependent KH vortex ring has highlighted the emergence of secondary elliptical and hyperbolic instabilities. They are named in reference to the local streamlines distribution and the associated deformation field in the region of the base flow where they develop. The former is localised in the KH vortex core where streamlines are locally elliptical in the frame of reference moving with the azimuthal vorticity maximum, whereas the latter yields oscillations in the braid region where streamlines are locally hyperbolic (in the same frame of reference). Following the work of Arratia, Caulfield & Chomaz (2013), they are referred to as E-type and H-type instabilities, respectively. Specifically, the E-type instability is a core-centred instability at small azimuthal wavenumber  $m \sim 1$ . The H-type instability, located on the braid, arises at larger wavenumbers  $m \gg 1$ . As advocated by Rogers & Moser (1993) in plane mixing layers, the three-dimensionalisation of homogeneous round jets thus results from the combined development of these two secondary instabilities whose relative contribution depends on the azimuthal wavenumber  $m$  and on the Reynolds number  $Re$  (Nastro *et al.* 2020). In free shear flows (jets, wakes and mixing layers), E-type and H-type instabilities are themselves found to grow thanks to a combination of the Orr (1907) and lift-up (Ellingsen & Palm 1975; Landhal 1975, 1980) transient mechanisms. Recently, the study of Jimenez-Gonzalez, Brancher & Martinez-Bazan (2015) on both the steady and the unsteady diffusing homogeneous jet profile showed the emergence of a third mechanism called ‘shift-up’. This phenomenon is of the same nature as the lift-up

mechanism because it is associated with a pair of counter-rotating streamwise vortices. Nevertheless, it is very specific to the helical perturbation ( $m = 1$ ) and induces a radial displacement of the jet as a whole.

In the case of a density-contrasted round jet, the presence of a density difference between the jet and the ambient flow substantially alters the KH vortex ring dynamics. We place ourselves in the case of round jets at large Froude numbers in the beyond-Boussinesq mixing regime. In this situation, when the jet-to-ambient density ratio  $S = \rho_j/\rho_\infty$  is below a critical threshold, the round jet exhibits self-sustained oscillations characterised by a synchronised train of KH billows at a well-marked frequency. This oscillating behaviour corresponds to the emergence of a nonlinear global axisymmetric mode of the jet (Lesshafft *et al.* 2006; Lesshafft, Huerre & Sagaut 2007) which has been observed experimentally both in heated jets by Monkewitz *et al.* (1990) and in binary mixing jets of helium–air by Kyle & Sreenivasan (1993). This global mode is the symptom of an absolute instability of the parallel flow within a sufficiently large streamwise extent starting from the nozzle exit (Lesshafft *et al.* 2006, 2007). This so-called *jet column mode* is different from the *shear-layer mode* associated with the classical KH instability because it exhibits a pressure disturbance extending well beyond the jet shear layer, with a maximum intensity on the jet axis (Jendoubi & Strykowski 1994). Its frequency is in good agreement with the Strouhal number of the global nonlinear mode close to the critical density ratio but departs significantly when  $S$  is decreased below this critical threshold (Lesshafft *et al.* 2006, 2007). In their experiments of heated jets, Monkewitz *et al.* (1990) identified two global modes with respective Strouhal numbers of  $St \sim 0.3$  and  $St \sim 0.45$  and corresponding to critical density ratios of  $S = 0.73$  and  $S = 0.63$ , whereas for helium–air jets, Kyle & Sreenivasan (1993) only observed the second mode with a frequency of  $St \sim 0.45$  below a density ratio of  $S = 0.6$ . Both the critical density ratio and the Strouhal number of this global mode depend on various physical parameters (Lesshafft *et al.* 2006; Lesshafft & Huerre 2007; Lesshafft *et al.* 2007; Nichols, Schmid & Riley 2007): the Reynolds number  $Re$ , the Mach number  $Ma$ , the jet aspect ratio  $\alpha = \ell_0/\vartheta$  where  $\ell_0$  is the jet radius and  $\vartheta$  is the shear layer momentum thickness and the density ratio  $S$  (only for the global frequency). Hallberg & Strykowski (2006) determined a universal scaling for the mode frequency  $St \sim Re \alpha^{1/2} (1 + S^{1/2})$  whereas the largest critical density ratio  $S = 0.73$  is obtained for incompressible jets at high aspect ratio and large Reynolds numbers (Monkewitz *et al.* 1990).

Another striking feature of low-density round jets lies in the spectacular side ejections, inclined and distinct from the main jet, that were first observed experimentally by Monkewitz & Bechert (1988) and Monkewitz *et al.* (1989). These side jets can exhibit ejection angles as large as  $90^\circ$  with respect to the jet axis and they induce an increase of the effluent to background fluid mixing and of the jet spreading. They are likely to be related to the development of secondary instabilities of low-density jets and there has been a consensus so far about the underlying physical mechanism that was first proposed by Monkewitz & Pfizenmaier (1991) and later supported by Brancher, Chomaz & Huerre (1994). This ejection mechanism relies on the amplification of radial velocity induction between pairs of counter-rotating longitudinal vortices that develop in between consecutive KH vortex rings. As such, the latter argument resorts to the intensification of a secondary perturbation that is already a standard pattern of the transition of homogeneous shear flows to three-dimensionality. The side ejections would not be driven then by any growth mechanism specific to variable-density flows. Because Monkewitz *et al.* (1989, 1990) observed these side ejections by heating or forcing acoustically the round jet, they were well-founded to consider side ejections as only by-products of the strong coherence of the self-sustained KH vortex rings either arising naturally below the critical density ratio or

due to the acoustic forcing. However, the experimental results of Fontane (2005) showed that side ejections could occur even if the density ratio is above the convective-absolute threshold, thus weakening the advocated causality between the existence of a global mode induced by an absolute primary instability and the existence of the side jets. In addition, Lopez-Zazueta, Fontane & Joly (2016), stemming from their stability analysis of the variable-density mixing layer, found that side jets may result from the convergence of longitudinal velocity streaks near the braid saddle point. This convergence is promoted by the linearised baroclinic torque contribution to the longitudinal velocity perturbation and stands as an alternative to the induction mechanism already present in the homogeneous situation. The physical mechanism at the origin of the side ejections thus remains an open question.

The dynamics of variable-density jets is affected by the baroclinic production/destruction of vorticity in response to the local misalignment between the density gradient, that scales with the Atwood number  $At = (S - 1)/(S + 1)$ , verifying  $At \in ] - 1, 1[$ , and the flow acceleration. Most importantly, Lesshafft & Huerre (2007) showed that the baroclinic torque is accountable for the change from a convective to an absolute nature of the jet column mode. In variable-density plane shear layers, the baroclinic vorticity production modifies significantly the secondary instabilities yielding a specific three-dimensionalisation associated with longitudinal velocity streaks in place of the pairs of counter-rotating longitudinal vortices arising in homogeneous shear flows (Lopez-Zazueta *et al.* 2016). In addition, a new secondary two-dimensional KH mode leading to fractal breakups has been also identified numerically (Reinaud, Joly & Chassaing 2000; Fontane, Joly & Reinaud 2008; Lopez-Zazueta *et al.* 2016). These secondary billows develop on the light side of the primary KH structure before being convected towards its core as the primary KH wave overturns.

For the purpose of clarifying the conjecture about the origin of the side ejections, we examine the secondary perturbation growth in the variable-density round jet. We thus perform a non-modal stability analysis over the unsteady evolution of the axisymmetric KH roll-up under substantial action of the density variation. Such analysis has not been conducted so far although several investigations on local and global modes were carried out for both the homogeneous (Garnaud *et al.* 2013*a,b*; Jimenez-Gonzalez *et al.* 2015; Jimenez-Gonzalez & Brancher 2017) and the variable-density unperturbed jet (Coenen *et al.* 2017). We set the Atwood number to  $|At| = 0.25$ , the negative and positive values corresponding to the light and heavy jets, respectively. As an illustration Atwood numbers  $At = -0.25$  and  $At = -0.28$  are representative of a jet of natural gas and a methane jet issuing in ambient air, and these are real situations in which mixing promotion may be sought. In addition, according to Fontane (2005), the corresponding density ratio  $S = 0.6$  is low enough to place ourselves in the domain of natural occurrence of side jets.

Adopting a temporal approach, non-parallel effects such as the frequency and wavenumber drifts are neglected. As the two-dimensional pairing is known to simply delay the progression towards the three-dimensionalisation of the flow (Moser & Rogers 1993; Rogers & Moser 1993; Arratia *et al.* 2013; Nastro 2020) but not to change the nature of the subsequent stages, we consider pairing-free base flows and we restrict the analysis to a time-dependent base flow with a streamwise extent coincident with the most amplified primary KH mode wavelength. We follow the time evolving process in a frame of reference moving with the constant phase velocity of the most unstable KH mode, with no bias on the outcome of the analysis but improving the observability of perturbations growth. The analysis addresses two distinct phases in the development of the base flow. The short-term dynamics for which the linear growth of the primary mode slightly alters the otherwise parallel base flow. In this first phase we also conduct a non-modal stability analysis of a

purely diffusing parallel jet, such as that carried out by Jimenez-Gonzalez *et al.* (2015) for the homogeneous jet. Then we consider optimal growth over the second phase that corresponds to the fully nonlinear roll-up into a vortex ring.

The paper is organised as follows. The governing equations and the numerical methods are presented in § 2 together with a detailed description of the specific features of the base flow that will influence the development of three-dimensional motions. The results are discussed in § 3 through the influence of the Atwood number  $At$ , the azimuthal wavenumber  $m$ , the optimisation interval (both the injection  $t_0$  and horizon  $T$  times) and the Reynolds number  $Re$ . Conclusions and perspectives are finally addressed and discussed in § 4.

## 2. Formulation of the problem

### 2.1. Governing equations

We consider a round jet of density  $\rho_j$  discharging into a quiescent fluid of density  $\rho_\infty$ . The reference frame is cylindrical  $(r, \theta, z)$  with the  $r$ ,  $\theta$  and  $z$  axes corresponding to the radial, azimuthal and streamwise directions, respectively. We denote  $\ell_0$ ,  $u_0$  and  $\rho_0$  the characteristic length, velocity and density scales. We take  $\ell_0$  as the jet radius,  $u_0$  as the jet centreline velocity and  $\rho_0$  as the mean density  $(\rho_j + \rho_\infty)/2$ . Considering an asymptotically small Mach number and constant dynamic viscosity  $\mu$  and Fickian diffusivity  $\mathcal{D}$ , which is a fair approximation for a binary mixing of perfect gases (see appendix A of Fontane 2005), the equation of state can be combined with the continuity equation and the transport equation of the mass fraction of one of the species to show that the non-solenoidal part of the velocity field is of diffusive nature (see Joseph 1990; Sandoval 1995):

$$\nabla \cdot \mathbf{u} = -\frac{1}{Re Sc} \nabla \cdot \left( \frac{1}{\rho} \nabla \rho \right), \quad (2.1)$$

where  $Re = (\rho_0 u_0 \ell_0) / \mu$  and  $Sc = \mu / \rho_0 \mathcal{D}$  are the Reynolds and Schmidt numbers. The relative weight of the inertia compared with buoyancy is measured by the Froude number  $Fr = u_0 / \sqrt{g' \ell_0}$  with the modified gravity acceleration being  $g' = gAt$ . As we address buoyancy-free flows, the Froude number is assumed to be large, i.e.  $Fr \gg 1$ , and the dimensionless Navier–Stokes equations read

$$D_t \rho = \frac{\rho}{Re Sc} \nabla \cdot \left( \frac{1}{\rho} \nabla \rho \right), \quad (2.2)$$

$$\rho D_t \mathbf{u} = -\nabla p + \frac{1}{Re} \Delta \mathbf{u} + \frac{1}{3Re} \nabla (\nabla \cdot \mathbf{u}), \quad (2.3)$$

where  $D_t = \partial_t + (\mathbf{u} \cdot \nabla)$  denotes the material derivative. The corresponding vorticity equation is obtained by taking the curl of the momentum equation (2.3)

$$\begin{aligned} D_t \boldsymbol{\omega} = & \boldsymbol{\omega} \cdot \nabla \mathbf{u} - \boldsymbol{\omega} (\nabla \cdot \mathbf{u}) + \frac{1}{\rho^2} \nabla \rho \times \nabla p \\ & + \frac{1}{Re \rho} \Delta \boldsymbol{\omega} - \frac{1}{Re \rho^2} \nabla \rho \times \Delta \mathbf{u} - \frac{1}{3Re \rho^2} \nabla \rho \times \nabla (\nabla \cdot \mathbf{u}), \end{aligned} \quad (2.4)$$

where the third term on the right-hand side is the baroclinic torque  $\mathbf{b} = (1/\rho^2) \nabla \rho \times \nabla p$  which becomes active as soon as isopycnals and isobars are not aligned. This source term plays a key role in the evolution of the variable-density base flow as shown in § 2.2.

As stated by (2.3) in the inviscid limit, the baroclinic torque can be rewritten by introducing the flow acceleration  $\mathbf{a} = D_t \mathbf{u} = -(1/\rho) \nabla p$ :

$$\mathbf{b} = \mathbf{a} \times \frac{1}{\rho} \nabla \rho, \tag{2.5}$$

which underlines the universal nature of baroclinic vorticity production. In large-Froude-number flows considered here, the local fluid particle acceleration  $\mathbf{a}$  replaces the constant external gravity acceleration  $\mathbf{g}$  relevant to low-Froude-number stratified flows.

### 2.2. Time-dependent variable-density KH vortex rings

The two-dimensional base flow consists in a time-evolving axisymmetric jet which undergoes the nonlinear development of the primary KH instability starting from the classical profile proposed by Michalke (1971). The velocity  $\mathbf{U} = [U_r, 0, U_z]$  and pressure fields  $P$  are computed in a meridian plane of extent  $[-r_{max}, r_{max}] \times [0, L_z]$  through a direct numerical simulation using a two-dimensional Fourier–Chebyshev pseudo-spectral method described in Joly, Fontane & Chassaing (2005), Joly & Reinaud (2007) and Nastro *et al.* (2020). We adopt a dealiased Fourier and a Chebyshev collocation method for the discretisation of the streamwise and radial directions, respectively. A free-slip boundary condition is imposed at the radial boundaries ( $r = \pm r_{max}$ ) of the flow domain, whereas the flow is periodic in the streamwise direction.

The velocity profile chosen for prescribing the initial condition corresponds to Michalke’s profile number two (Michalke 1971) and the initial density profile is assumed to have the same functional form (see Fontane 2005; Nichols *et al.* 2007):

$$\bar{U}_z(r) = \frac{1}{2} + \frac{1}{2} \tanh \left[ \frac{\alpha}{4} \left( \frac{1}{r} - r \right) \right], \tag{2.6}$$

$$\bar{R}(r) = 1 + \frac{At}{1 - At} \left\{ 1 + \tanh \left[ \frac{\alpha_\rho}{4} \left( \frac{1}{r} - r \right) \right] \right\}, \tag{2.7}$$

where  $\alpha = \ell_0/\vartheta$  is the jet aspect ratio with  $\vartheta$  the shear layer momentum thickness and  $\alpha_\rho = \ell_0/\vartheta_\rho$  is the aspect ratio of the density profile where  $\vartheta_\rho$  represents the gradient density thickness. For comparison with the results of Nastro (2020) in the homogeneous case, the aspect ratio  $\alpha$  of the velocity profile is set at  $\alpha = 10$  throughout this paper. This choice stems from the fact that this value stands as an intermediate value and allows to gather the specific features of the cylindrical geometry. It should be recalled that for  $\alpha \gg 1$  the shear layer momentum thickness  $\vartheta$  is significantly small compared with the jet radius  $\ell_0$ , so that the flow development is not significantly affected by the cylindrical geometry, whereas for  $\alpha \lesssim 9.5$  the Michalke profile is susceptible to host naturally a helical primary KH mode rather than the axisymmetric one (Jimenez-Gonzalez *et al.* 2015). Moreover, we consider  $\vartheta_\rho \equiv \vartheta$  so that the density aspect ratio coincides with the radius-to-momentum thickness ratio, i.e.  $\alpha_\rho \equiv \alpha = 10$ . Two distinct base flows are generated for the transient growth analysis over short times. First, the time evolution of a purely diffusive unperturbed parallel jet is obtained by initialising the direct numerical simulation with the velocity and density fields (2.6)–(2.7). Second, the nonlinear KH roll-up is obtained by perturbing the axisymmetric jet defined by (2.6)–(2.7) with the most unstable mode given by the temporal linear stability analysis, i.e. the primary KH mode (see Nastro *et al.* 2020). The superposition of the Michalke profiles and the primary KH mode (scaled by a small amplitude  $a_{KH}$ ) stands as the initial condition for the direct

$At$	$S = \rho_j/\rho_\infty$	$\ell_0$	$\vartheta c_{iKH}$	$c_{rKH}$	$r_{max}$	$100a_{KH}$	$L_z/\ell_0$	$\Delta\mathcal{G}_E _{t \rightarrow \infty}$
-0.25	0.600	2.34	0.0444	0.562	16.4	1.43	2.69	2.05
0	1	2.39	0.0421	0.633	16.7	1.88	2.63	2.17
0.25	1.667	2.60	0.0410	0.689	18.2	1.98	2.42	2.38

Table 1. Main numerical parameters for the simulated KH base flow fields: Atwood number  $At$ ; density ratio  $S = \rho_j/\rho_\infty$ ; jet radius  $\ell_0$ ; growth rate  $c_{iKH}$  and phase velocity  $c_{rKH}$  of the primary KH mode; maximum radius  $r_{max}$ ; initial amplitude of the KH mode  $a_{KH}$ ; ratio  $L_z/\ell_0$  between the domain streamwise extent and the jet radius; and asymptotic additional energy gain  $\Delta\mathcal{G}_E|_{t \rightarrow \infty}$  according to equation (A23) of Ortiz & Chomaz (2011).

numerical simulation. Due to nonlinearities, the energy of the primary KH mode reaches a maximum at the so-called saturation time  $T_s$  that depends on the amplitude  $a_{KH}$ , the flow dimensionless parameters ( $Re$ ,  $Sc$  and  $At$ ) and the aspect ratio  $\alpha$ . The saturation time also depends on the nature of the initial perturbation. We arbitrarily choose to seed the base flow with the most amplified KH mode. We could have chosen to seed the base flow with the optimal KH disturbance but it has been demonstrated in the homogeneous case that the optimal secondary growth stays unaffected (Nastro 2020). The Reynolds number is set to  $Re = 1000$  (except in §§ 3.3 and 3.4, where its influence is considered), which is large enough to ensure that the primary KH wave wraps itself into a finite-amplitude energetic vortex ring. This value of the Reynolds number is representative of the values for which side jets naturally arise in light jets (Fontane 2005). The Schmidt number is fixed to  $Sc = 1$  which is relevant for the binary mixing of perfect gases, as shown by Fontane (2005). The initial amplitude  $a_{KH}$  is set to ensure the existence of the same significant linear phase of growth for all cases, i.e.  $\alpha T_s = 100$ . The jet radius  $\ell_0$  is set so that the most amplified KH mode corresponds to a wavenumber of  $2\pi/L_z$  and the radial extent of the domain is chosen as  $r_{max} = 7\ell_0$ . It has been checked to be large enough to ensure no influence of the free-slip boundary condition on the flow evolution. For all simulations, we use a mesh of  $512^2$  points, which guarantees the numerical convergence of the results. All the numerical settings for the variable-density KH base flow fields are summarised in table 1. Furthermore, the long-term additional energy gain  $\Delta\mathcal{G}_E|_{t \rightarrow \infty}$  related to the primary direct/adjoint KH modes is evaluated through the asymptotic prediction of Ortiz & Chomaz (2011) and is given in table 1. As the additional gain becomes larger as  $At$  increases, it can be stated that the transient energy growth of the optimal KH excitation is stronger for the heavy jet than for the light one. However, as already observed by Fontane (2005), the growth rate of the direct KH mode developing over a light jet is significantly higher than that measured for a heavy jet.

Because the structure of the base flow has a direct influence on the characteristics of the secondary instabilities, the specific features of the variable-density KH vortex ring are described and compared with its homogeneous counterpart. Figure 1 displays the spatial structure of the baroclinic torque at the saturation time  $T_s$  for an Atwood number of  $At = -0.25$  and  $At = 0.25$ . It is mostly active along the braid in the form of a source–sink dipole centred on the hyperbolic saddle point H. The inviscid expression (2.5) is used to illustrate the local combination of acceleration and density-gradient yielding the two main vorticity sources and sinks along the braid. Due to the kinematic blockage born by the vicinity of the jet axis, the local acceleration field  $a$  is not symmetric with respect to the elliptical stagnation point E unlike in the plane mixing-layer configuration. The base flow acceleration is stronger on the side of the braid drifting away from the jet

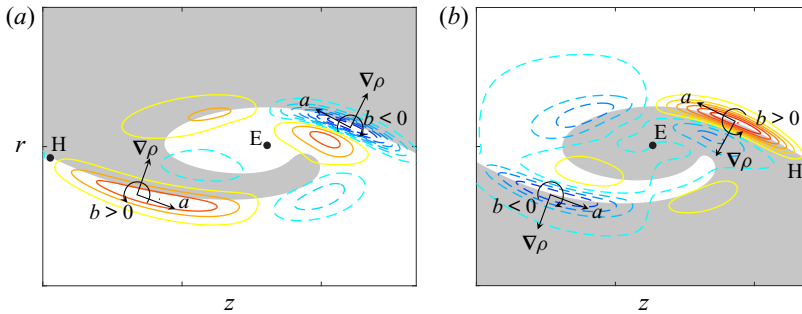


Figure 1. Baroclinic torque distribution for a KH vortex ring at saturation time developing on (a) a light jet with  $At = -0.25$  and (b) a heavy one with  $At = 0.25$ . Points H and E denote the hyperbolic and elliptical stagnation points. The grey-shaded region corresponds to the domain where the base flow density is higher than  $\rho_0$ . Solid (dashed) contours correspond to positive (negative) values of the contoured quantity (here the baroclinic torque). Only the upper half-plane is shown and the jet axis corresponds to the lower bound. These conventions hold throughout the paper.

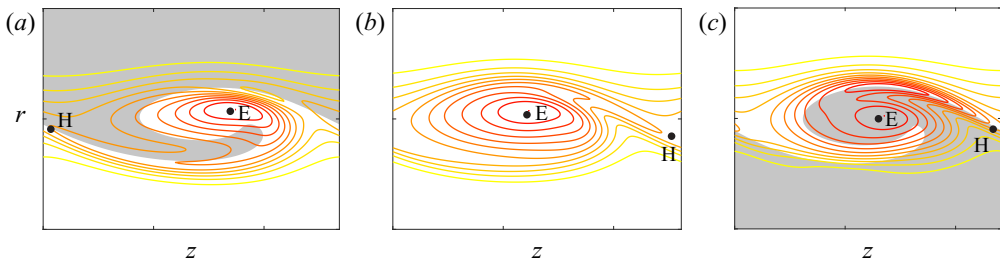


Figure 2. Azimuthal vorticity field of a KH vortex ring at the KH saturation time  $T_s$  for (a)  $At = -0.25$ , (b)  $At = 0$  and (c)  $At = 0.25$ .

axis, i.e. the outer side, than that on the side of the braid pointing towards the axis, i.e. the inner side. This results in a non-zero net balance of the baroclinic sources/sinks in the jet half-plane. In the following statements, baroclinic azimuthal vorticity production refers to a contribution of the same sign as the initial vorticity, and of opposite sign for destruction. As illustrated in [figure 1\(a\)](#) for the light jet, the resulting baroclinic vorticity destruction is larger than the baroclinic production. The reverse is true for the heavy jet with a stronger vorticity production than the destruction, as shown in [figure 1\(b\)](#). Importantly enough, these uneven contributions of the baroclinic torque emphasise the loss of central symmetry with respect to the elliptical stagnation point already observable in the homogeneous jet. This is illustrated in [figure 2](#) which displays the azimuthal vorticity field of a KH vortex ring at the saturation time  $T_s$  for the light, homogeneous and heavy jets. In agreement with [figure 1](#), a significant depletion of base flow vorticity is observed on the outer side of the braid of the light jet, together with a slight increase of vorticity on the inner side. In the heavy jet, the local baroclinic production on the outer side of the braid yields a local maximum of vorticity of the same magnitude as that located in the vortex core. The deformation of the isocontours on the inner side of the heavy jet braid denotes a substantial local reduction of the azimuthal vorticity. This uneven redistribution of vorticity is intensified with increasing Atwood and Reynolds numbers as illustrated by the azimuthal vorticity of the same variable-density jets at  $Re = 10\,000$  in [figure 3](#). Increasing the Reynolds number results in sharper gradients of velocity and density which



Optimal growth over a time-evolving VD jet at  $|At| = 0.25$

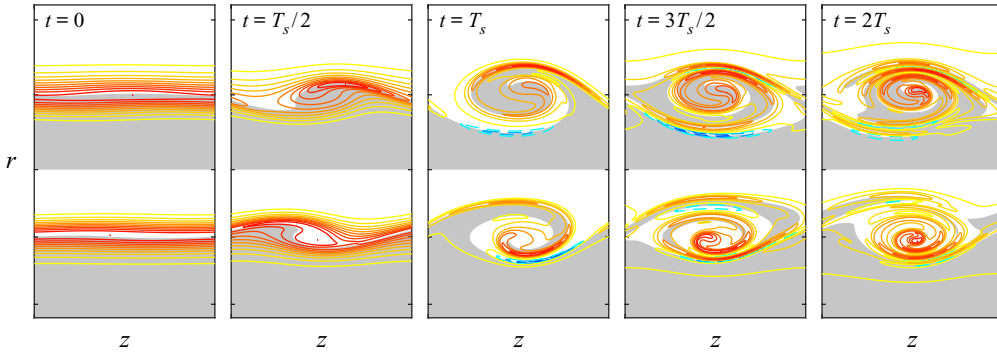


Figure 3. Temporal evolution of the azimuthal vorticity field of a perturbed round jet for  $Re = 10\,000$  with  $At = -0.25$  (lower half-plane) and  $At = 0.25$  (upper half-plane). When comparing in the entire meridional plane, the jet axis lies in the centre of the figure and this convention holds throughout the paper.

yield a layered distribution of the base flow vorticity as well as stronger baroclinic sources and sinks. Their effect on the base flow is visible at the saturation time where vorticity patches of opposite sign are observable on the inner side of the braid for the heavy jet and on the outer side for the light one.

Another consequence, closely related to the base flow vorticity redistribution, lies in a significant change in the strain field. Figure 4 shows the local distribution of the Euclidean norm of the deviatoric strain rate tensor  $\|\mathbf{D}_0\|_2$  for  $t = 0.8T_s, T_s, 1.2T_s$  (see Appendix A for its definition). Before the KH saturation time, the maximum of the strain rate field is located in the braid region. For the light jet, it spreads also towards the vortex core and its magnitude is slightly lower than those observed for the homogeneous and heavy cases. At the saturation time, the light jet exhibits a strong intensification of its strain rate field in a region going from the vortex core to the outer side of the braid. A similar but less intense trend is observed in the homogeneous case. For the heavy jet ( $At = 0.25$ ), the strain rate field remains concentrated within the outer side of the braid, i.e. in the same region where the baroclinic torque is an active source term (see also figure 1b). After the KH saturation, i.e.  $t = 1.2T_s$ , the magnitude of the strain rate in the light jet becomes significantly larger than those of the homogeneous and heavy cases and peaks in a narrow zone located in the outer part of the vortex ring between the elliptical and hyperbolic stagnation points.

### 2.3. Optimisation problem

The linear evolution of the three-dimensional perturbations  $[\mathbf{u}, \rho, p]$  that are likely to develop on the top of the variable-density KH vortex ring  $[U, R, P]$  is now considered. We linearise the governing equations (2.1)–(2.3) around the two-dimensional base flow and we retain only the equations for the small-amplitude perturbations:

$$\frac{\partial \rho}{\partial t} = -(\mathbf{U} \cdot \nabla \rho + \mathbf{u} \cdot \nabla R) - \rho(\nabla \cdot \mathbf{U}) - R(\nabla \cdot \mathbf{u}), \quad (2.8)$$

$$\begin{aligned} \frac{\partial \mathbf{u}}{\partial t} = & -(\mathbf{U} \cdot \nabla \mathbf{u} + \mathbf{u} \cdot \nabla \mathbf{U}) - \frac{1}{R} \nabla p + \frac{\rho}{R^2} \nabla P + \frac{1}{ReR} \Delta \mathbf{u} \\ & - \frac{\rho}{ReR^2} \Delta \mathbf{U} + \frac{1}{3ReR} \nabla(\nabla \cdot \mathbf{u}) - \frac{\rho}{3ReR^2} \nabla(\nabla \cdot \mathbf{U}), \end{aligned} \quad (2.9)$$

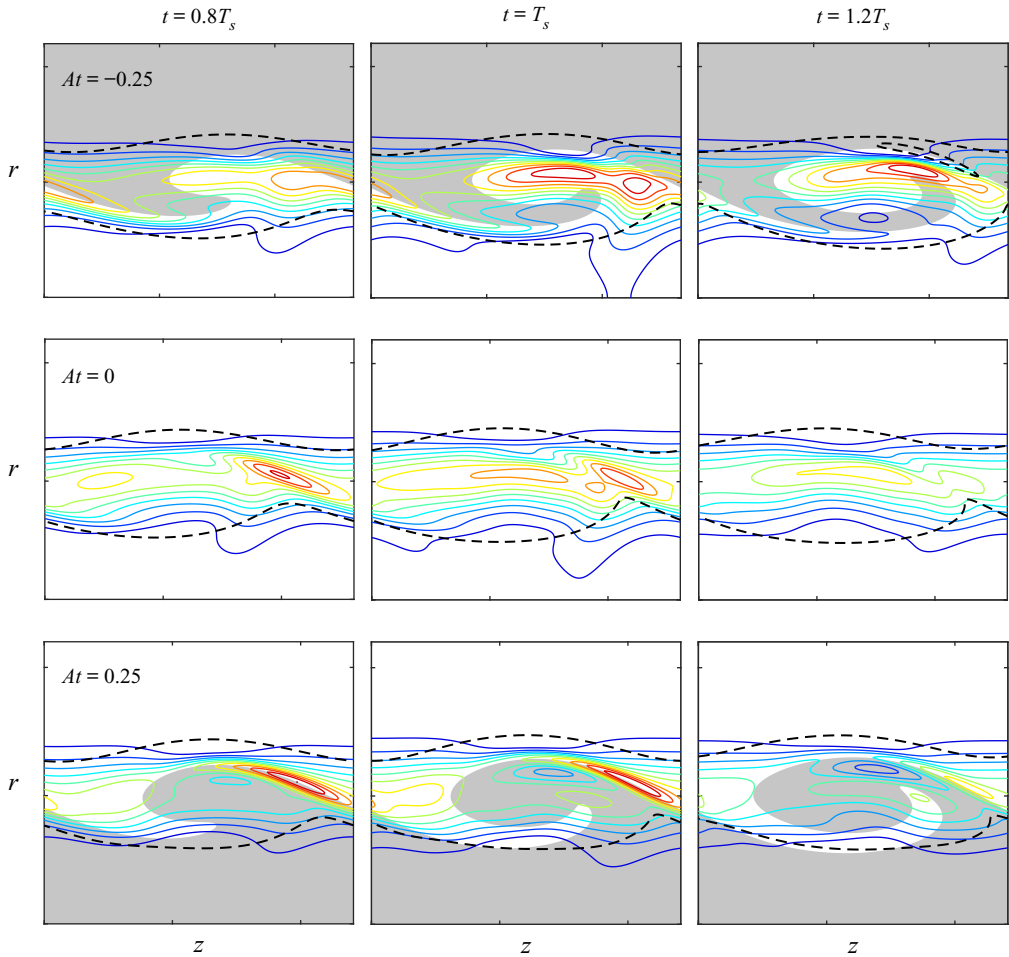


Figure 4. Euclidean norm of the deviatoric strain rate tensor in the time interval  $[0.8T_s, 1.2T_s]$  for  $At = -0.25, 0, 0.25$  and  $Re = 1000$ . Dashed contours correspond to 20% of the maximal absolute value of the base flow azimuthal vorticity  $\Omega_\theta$ . The contour levels are the same for all figures.

$$\nabla \cdot \mathbf{u} = -\frac{1}{ReSc} \Delta \left( \frac{\rho}{R} \right). \quad (2.10)$$

This linear system, referred to as the direct system, can be cast in the following compact form:

$$\mathbf{N}_t \cdot \mathbf{q} + \mathbf{N}_c \cdot \mathbf{q} + \frac{1}{Re} \mathbf{N}_d \cdot \mathbf{q} = 0, \quad (2.11)$$

where  $\mathbf{q} = [\mathbf{u}, \rho, p]$  and the three matrix operators are the temporal operator  $\mathbf{N}_t$ , the operator of coupling between the base flow and the perturbation  $\mathbf{N}_c$  and the diffusion operator  $\mathbf{N}_d$ , respectively. Their expressions are detailed in [Appendix B](#).

In the frame of non-modal stability analysis, the temporal behaviour of the perturbations is not prescribed and, considering the streamwise periodicity and the azimuthal homogeneity of the base flow, the disturbances are sought under the form

$$[u_r, u_\theta, u_z, \rho, p](r, \theta, z, t) = \frac{1}{2}([\tilde{u}_r, i\tilde{u}_\theta, \tilde{u}_z, \tilde{\rho}, \tilde{p}](r, z, t) e^{i(\mu z + m\theta)} + \text{c.c.}), \quad (2.12)$$

where  $m$  is the azimuthal wavenumber and  $\mu \in [0, 1]$  the real Floquet exponent. We restrict here the search for perturbations that have the same streamwise periodicity as the base flow, i.e.  $\mu = 0$ . This is motivated by the experimental evidence that three-dimensional secondary instabilities involved in round jets develop in between two consecutive KH vortex rings. Furthermore, Klaassen & Peltier (1991) and Fontane & Joly (2008) found that the most unstable modes of both stratified and inhomogeneous mixing layers did not vary appreciably with non-zero Floquet exponent.

Amongst all possible perturbations likely to grow over the KH vortex ring, we look for those maximising the gain of kinetic energy  $E$  over a prescribed period of time  $[t_0, T]$ :

$$G_E(T, t_0) = \frac{E(T)}{E(t_0)} = \frac{\|q(T)\|_u}{\|q(t_0)\|_u}, \quad (2.13)$$

where  $t_0, T$  are called the injection and horizon times, respectively, and  $\|\cdot\|_u$  denotes the seminorm associated with the conventional inner product yielding the kinetic energy (see Appendix C). Following the work of Farrell (1988), we look for the optimal perturbation with the maximal energy gain

$$\mathcal{G}_E(T, t_0) = \max_{q(t_0)} \{G_E(T, t_0)\}, \quad (2.14)$$

over all the possible initial conditions  $q(t_0)$ . Its determination resorts to solving an optimisation problem with constraints (Gunzburger 2002) enforcing the perturbation to be a solution of the linearised Navier–Stokes equations (2.11). The problem can be classically transformed into an optimisation problem without constraint using the variational method of the Lagrange multipliers (see Luchini & Bottaro 1998; Corbett & Bottaro 2000, 2001). This requires the derivation of the so-called adjoint equations (Schmid 2007) associated with the direct system (2.8)–(2.9):

$$-\frac{\partial \rho^\dagger}{\partial t} = U \cdot \nabla \rho^\dagger + \frac{1}{R^2} u^\dagger \cdot \left[ \nabla P - \frac{1}{Re} \Delta U - \frac{1}{3Re} \nabla (\nabla \cdot U) \right] - \frac{1}{ReScR} \Delta p^\dagger, \quad (2.15)$$

$$-\frac{\partial u^\dagger}{\partial t} = [U \cdot \nabla u^\dagger + u^\dagger (\nabla \cdot U) - u^\dagger \cdot \nabla U^T] + \nabla p^\dagger + R \nabla \rho^\dagger + \frac{1}{Re} \Delta \left( \frac{u^\dagger}{R} \right) + \frac{1}{3Re} \nabla \left[ \nabla \cdot \left( \frac{u^\dagger}{R} \right) \right], \quad (2.16)$$

$$\nabla \cdot \left( \frac{u^\dagger}{R} \right) = 0. \quad (2.17)$$

Likewise the direct system (2.11), the adjoint system can be reduced to the following compact form:

$$-N_t \cdot q^\dagger + N_c^\dagger \cdot q^\dagger + \frac{1}{Re} N_d^\dagger \cdot q^\dagger = 0, \quad (2.18)$$

where  $q^\dagger = [u^\dagger, \rho^\dagger, p^\dagger]$ . Solving the evolution of this dynamical system requires a backward-in-time integration as signified by the minus sign before the temporal operator  $N_t$ . The expressions for the adjoint matrix operator  $N_c^\dagger$  of the coupling between the base flow and the disturbance and the adjoint diffusion operator  $N_d^\dagger$  are given in Appendix B. An iterative procedure allows to determine the optimal perturbation and the corresponding optimal energy gain  $\mathcal{G}_E$ , as originally proposed by Luchini & Bottaro (2001) and Corbett & Bottaro (2001). An initial condition  $q(t_0)$  chosen as a white noise is integrated forward

in time to the horizon time  $T$  using the direct system (2.11). The initial white noise condition can be applied to every field of the perturbation, but we restrict it here to the velocity field because the objective is to maximise the kinetic energy gain from a purely kinematic initial perturbation. The resulting final state is used to compute the initial condition  $\mathbf{q}^\dagger(T)$  for the adjoint system (2.18) which is integrated backward-in-time back to the injection time  $t_0$ . After an appropriate normalisation, this perturbation candidate at  $t_0$  is used as the initial condition for the next direct-adjoint integration. Multiple iterations of this forward–backward loop converge eventually to the optimal perturbation. Both direct and adjoint systems are integrated with the linearised version of the two-dimensional three-components dealiased pseudo-spectral method used for the generation of the base flow. The outline of the optimisation algorithm is given in Appendix C and full details are provided in § 2.3.3 of Nastro (2020). In practice, the convergence of this iterative optimisation algorithm is very quick and the solution is currently obtained in about 10 iterations.

### 2.4. Diagnostics

In order to understand the physical mechanisms associated with the energy growth of the optimal perturbations, we use diagnostics such as the evolution equation for the energy growth rate of the perturbation  $\sigma_E = (1/E) dE/dt$ . It is obtained straightforwardly from the transport equation for the perturbation kinetic energy  $E = \|\mathbf{q}\|_u$  which reads

$$\begin{aligned} \frac{dE}{dt} = & - \underbrace{\int_{\mathcal{V}} u_r u_z \left( \frac{\partial U_r}{\partial z} + \frac{\partial U_z}{\partial r} \right) d\mathcal{V}}_{\Pi_{E_1}} - \underbrace{\int_{\mathcal{V}} \left( u_r^2 \frac{\partial U_r}{\partial r} + u_\theta^2 \frac{U_r}{r} + u_z^2 \frac{\partial U_z}{\partial z} \right) d\mathcal{V}}_{\Pi_{E_2}} \\ & + \underbrace{\int_{\mathcal{V}} \frac{\|\mathbf{u}\|}{2} (\nabla \cdot \mathbf{U}) d\mathcal{V}}_{\Pi_{E_3}} - \underbrace{\int_{\mathcal{V}} \left( \frac{\mathbf{u}}{R} \cdot \nabla p \right) d\mathcal{V}}_{\Pi_{E_4}} + \underbrace{\int_{\mathcal{V}} \frac{\rho}{R^2} \left( \frac{\mathbf{u}}{R} \cdot \nabla P \right) d\mathcal{V}}_{\Pi_{E_5}} \\ & + \underbrace{\frac{1}{Re} \int_{\mathcal{V}} \phi_\mu d\mathcal{V}}_{\Pi_{E\phi_1}} + \underbrace{\frac{1}{Re} \int_{\mathcal{V}} \Phi_\mu d\mathcal{V}}_{\Pi_{E\phi_2}}, \end{aligned} \tag{2.19}$$

where  $\phi_\mu$  is the viscous dissipation coming from the perturbation velocity field defined by

$$\phi_\mu = \frac{1}{R} \left\{ \mathbf{u} \cdot \Delta \mathbf{u} + \frac{1}{3} [\mathbf{u} \cdot \nabla (\nabla \cdot \mathbf{u})] \right\}, \tag{2.20}$$

and  $\Phi_\mu$  is the viscous dissipation coming from the coupling with the base flow velocity field defined by

$$\Phi_\mu = -\frac{\rho}{R^2} \left\{ \mathbf{u} \cdot \Delta \mathbf{U} + \frac{1}{3} [\mathbf{u} \cdot \nabla (\nabla \cdot \mathbf{U})] \right\}. \tag{2.21}$$

Different source/sink terms can be thus distinguished in (2.19):  $\Pi_{E_1}$  is the energy production/destruction due to the base flow shear,  $\Pi_{E_2}$  the energy production/destruction due to the base flow strain field,  $\Pi_{E_3}$  the energy production/destruction due to the base flow dilatation,  $\Pi_{E_4}$  the energy production/destruction due to the perturbation pressure gradient,  $\Pi_{E_5}$  the energy production/destruction due to the base flow pressure gradient,  $\Pi_{E\phi_1}$  the viscous dissipation coming from the perturbation velocity field and  $\Pi_{E\phi_2}$  the

viscous dissipation involving the base flow velocity field. The terms  $\Pi_{E_3}$ ,  $\Pi_{E_4}$ ,  $\Pi_{E_5}$  and  $\Pi_{E\phi_2}$  are specific to the variable-density case, and both  $\Pi_{E_4}$  and  $\Pi_{E_5}$  terms correspond to the remnant of the baroclinic vorticity production in the kinetic energy equation.

It is also useful to derive the linearised version of the vorticity equation (2.4) which reads

$$\frac{\partial \boldsymbol{\omega}}{\partial t} + \mathbf{U} \cdot \nabla \boldsymbol{\omega} + \mathbf{u} \cdot \nabla \boldsymbol{\Omega} = \boldsymbol{\Omega} \cdot \nabla \mathbf{u} + \boldsymbol{\omega} \cdot \nabla \mathbf{U} - \boldsymbol{\Omega}(\nabla \cdot \mathbf{u}) - \boldsymbol{\omega}(\nabla \cdot \mathbf{U}) + \mathbf{b} + \frac{1}{ReR} \left( \Delta \boldsymbol{\omega} - \frac{\rho}{R} \Delta \boldsymbol{\Omega} - \boldsymbol{\phi}_R - \boldsymbol{\phi}_\rho \right), \quad (2.22)$$

where  $\mathbf{b}$  is the linearised baroclinic torque defined by

$$\mathbf{b} = \frac{1}{R} \nabla R \times \underbrace{\left( \frac{1}{R} \nabla p - \frac{\rho}{R^2} \nabla P \right)}_{(i)} + \nabla \left( \frac{\rho}{R} \right) \times \underbrace{\frac{1}{R} \nabla P}_{(ii)}, \quad (2.23)$$

$\boldsymbol{\phi}_R$  and  $\boldsymbol{\phi}_\rho$  are the coupling between the base flow density field and the perturbation diffusion and the coupling between the perturbation density field and the base flow diffusion, respectively. They are defined as follows:

$$\boldsymbol{\phi}_R = \frac{1}{R} \nabla R \times \left( \mathcal{F}_D - \frac{\rho}{R} \mathcal{F}_D \right), \quad (2.24)$$

$$\boldsymbol{\phi}_\rho = \nabla \left( \frac{\rho}{R} \right) \times \mathcal{F}_D, \quad (2.25)$$

where  $\mathcal{F}_D = \Delta \mathbf{U} + \frac{1}{3} \nabla(\nabla \cdot \mathbf{U})$  and  $\mathcal{f}_D = \Delta \mathbf{u} + \frac{1}{3} \nabla(\nabla \cdot \mathbf{u})$ .

As already done for the baroclinic torque (2.5) in the base flow vorticity equation, the pressure terms (i) and (ii) in (2.23) can be replaced by the flow accelerations in the limit of  $Re \rightarrow \infty$

$$\mathbf{b} = \mathbf{a} \times \frac{1}{R} \nabla R + \mathbf{A} \times \nabla \left( \frac{\rho}{R} \right) \quad (2.26)$$

with  $\mathbf{a}$  and  $\mathbf{A}$  the perturbation and base flow accelerations:

$$\mathbf{a} = \frac{\partial \mathbf{u}}{\partial t} + \mathbf{U} \cdot \nabla \mathbf{u} + \mathbf{u} \cdot \nabla \mathbf{U} = -\frac{1}{R} \nabla p + \frac{\rho}{R^2} \nabla P, \quad (2.27a)$$

$$\mathbf{A} = \frac{\partial \mathbf{U}}{\partial t} + \mathbf{U} \cdot \nabla \mathbf{U} = -\frac{1}{R} \nabla P. \quad (2.27b)$$

The equation for the perturbation enstrophy  $Z = \int_{\mathcal{V}} \boldsymbol{\omega}^* \cdot \boldsymbol{\omega} d\mathcal{V}$  is derived from the vorticity transport equation (2.22) to evaluate its growth rate  $\sigma_Z = (1/Z) dZ/dt$  budget:

$$\begin{aligned} \frac{dZ}{dt} = & \underbrace{\int_{\mathcal{V}} \omega_r \omega_z \left( \frac{\partial U_r}{\partial z} + \frac{\partial U_z}{\partial r} \right) d\mathcal{V}}_{\Pi_{Z_1}} + \underbrace{\int_{\mathcal{V}} \left( \omega_r^2 \frac{\partial U_r}{\partial r} + \omega_\theta^2 \frac{U_r}{r} + \omega_z^2 \frac{\partial U_z}{\partial z} \right) d\mathcal{V}}_{\Pi_{Z_2}} \\ & - \underbrace{\int_{\mathcal{V}} \frac{\|\boldsymbol{\omega}\|^2}{2} (\nabla \cdot \mathbf{U}) d\mathcal{V}}_{\Pi_{Z_3}} - \underbrace{\int_{\mathcal{V}} [\boldsymbol{\omega} \cdot (\mathbf{u} \cdot \nabla \boldsymbol{\Omega})^T] d\mathcal{V}}_{\Pi_{Z_4}} + \underbrace{\int_{\mathcal{V}} [\boldsymbol{\omega} \cdot (\boldsymbol{\Omega} \cdot \nabla \mathbf{u})^T] d\mathcal{V}}_{\Pi_{Z_5}} \end{aligned}$$

$$- \underbrace{\int_{\mathcal{V}} (\boldsymbol{\omega} \cdot \boldsymbol{\Omega})(\nabla \cdot \mathbf{u}) \, d\mathcal{V}}_{\Pi_{Z_6}} + \underbrace{\int_{\mathcal{V}} (\boldsymbol{\omega} \cdot \mathbf{b}) \, d\mathcal{V}}_{\Pi_{Z_7}} + \underbrace{\frac{1}{Re} \int_{\mathcal{V}} \phi_Z \, d\mathcal{V}}_{\Pi_{Z_{\phi_1}}} + \underbrace{\frac{1}{Re} \int_{\mathcal{V}} \Phi_Z \, d\mathcal{V}}_{\Pi_{Z_{\phi_2}}}, \quad (2.28)$$

where

$$\phi_Z = \frac{1}{R} [\boldsymbol{\omega} \cdot (\boldsymbol{\Delta} \boldsymbol{\omega} - \boldsymbol{\phi}_\rho)] \quad \text{and} \quad \Phi_Z = -\frac{\rho}{R^2} \left[ \boldsymbol{\omega} \cdot \left( \boldsymbol{\Delta} \boldsymbol{\Omega} + \frac{R}{\rho} \boldsymbol{\phi}_R \right) \right]. \quad (2.29a,b)$$

In particular, we can distinguish different source/sink terms in (2.28):  $\Pi_{Z_1}$  is the enstrophy production/destruction due to the base flow shear,  $\Pi_{Z_2}$  the enstrophy production/destruction due to the base flow strain,  $\Pi_{Z_3}$  the enstrophy production/destruction due to the base flow dilatation,  $\Pi_{Z_4}$  the enstrophy production/destruction due to the perturbation stretching,  $\Pi_{Z_5}$  the enstrophy production/destruction due to the base flow vorticity advection,  $\Pi_{Z_6}$  the enstrophy production/destruction due to the perturbation dilatation,  $\Pi_{Z_7}$  is the baroclinic enstrophy production/destruction,  $\Pi_{Z_{\phi_1}}$  the viscous dissipation coming from the perturbation vorticity field and  $\Pi_{Z_{\phi_2}}$  the viscous dissipation resulting from the base flow vorticity field.

### 3. Optimal perturbations in variable-density jets

#### 3.1. The universal first phase

We first consider the early evolution of optimal perturbations growing from the initial time of the base flow evolution, i.e.  $t_0 = 0$ , on both an unperturbed parallel jet experiencing viscous spreading and a jet perturbed by a low-amplitude KH mode. The Reynolds number is  $Re = 1000$  and the Atwood number is  $At = -0.25$  and  $At = 0.25$  for the light and heavy jets, respectively. Figure 5 displays the temporal evolution of the energy gain  $\mathcal{G}_E$  of perturbations optimised for  $T = T_s/2$  and  $T = T_s$ , for azimuthal wavenumbers ranging from  $m = 0$  to  $m = 5$ . The time variable is normalised by the KH saturation time  $T_s$ . For comparison, the energy gains corresponding to the homogeneous case have been added (Jimenez-Gonzalez *et al.* 2015; Nastro *et al.* 2020). When perturbations are optimised for half the KH saturation time, the energy curves are all superimposed reaching a value of  $\mathcal{G}_E \approx 10^2$ , whether disturbances grow over an unperturbed or a perturbed jet. In the interval  $[0, T_s/2]$ , the Atwood number does not have much influence on the perturbation growth either, because the energy gain follows the same route for all cases. For  $t > T_s/2$ , the optimal growth becomes more sensitive to the Atwood number as the energy evolution corresponding to the light and heavy jets slightly deviate from the one of the homogeneous case. The difference between the perturbed and unperturbed jet base flows becomes also perceptible after half the KH saturation time. For this reason, we consider  $T_s/2$  as a milestone that separates the evolution of optimal disturbances in two periods: an initial time interval  $[0, T_s/2]$  characterised by a universal growth of the perturbation energy regardless of the density variations and the low-amplitude KH wave, and a second period starting at  $t \approx T_s/2$  when the evolution of the optimal perturbation starts becoming sensitive to the Atwood number and the nonlinear development of the KH mode. This initial energy growth has been recognised to be universal in all shear flows by Farrell & Ioannou (1993) and has also been observed in the case of variable-density mixing layers (Lopez-Zazueta *et al.* 2016). It is associated with energy growth driven by a combination of Orr and lift-up mechanisms, as discussed in the following.

We now focus on the spatial distribution of the kinetic energy of perturbations optimised for  $T = T_s/2$ . Figure 6(a) shows the temporal evolution of the kinetic energy field  $E$  from

Optimal growth over a time-evolving VD jet at  $|At| = 0.25$

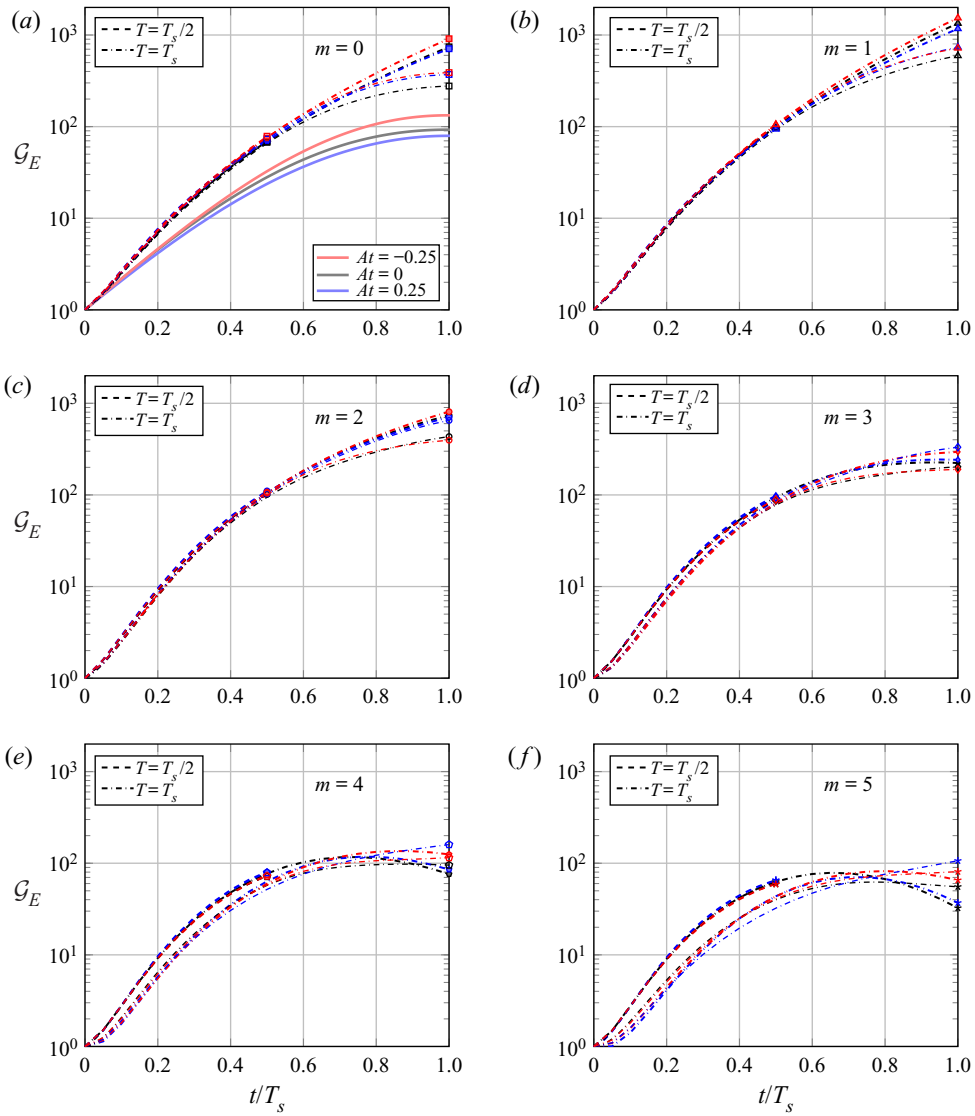


Figure 5. Temporal evolution of the energy gain  $\mathcal{G}_E$  for optimal perturbations growing over a diffusing Michalke profile (thick lines) and over a perturbed jet (thin lines) for  $At = -0.25$  (red),  $At = 0$  (black) and  $At = 0.25$  (blue) and six azimuthal wavenumbers  $m \in [0; 5]$ . The thick continuous lines in the figure corresponding to  $m = 0$  represent the temporal evolution of the energy gain of the primary KH modes. The symbols are located at the horizon time of each energy curve.

the injection time  $t_0 = 0$  to  $T = T_s/2$  for the optimal perturbation growing over a parallel jet under viscous spreading (lower half-plane) and a jet perturbed by the KH mode (upper half-plane), both in the light jet case at  $At = -0.25$ . We consider the same values of azimuthal wavenumber  $m$  as in figure 5. Figure 6(b) displays similarly the kinetic energy of optimal perturbations in the case of a heavy jet characterised by  $At = 0.25$ . At injection time, the optimal perturbations take the form of two elongated layers oriented along the direction of maximal compression of the base flow very similar to those observed in the homogeneous case (see Nastro *et al.* 2020). In the diffusing parallel jet, these structures are

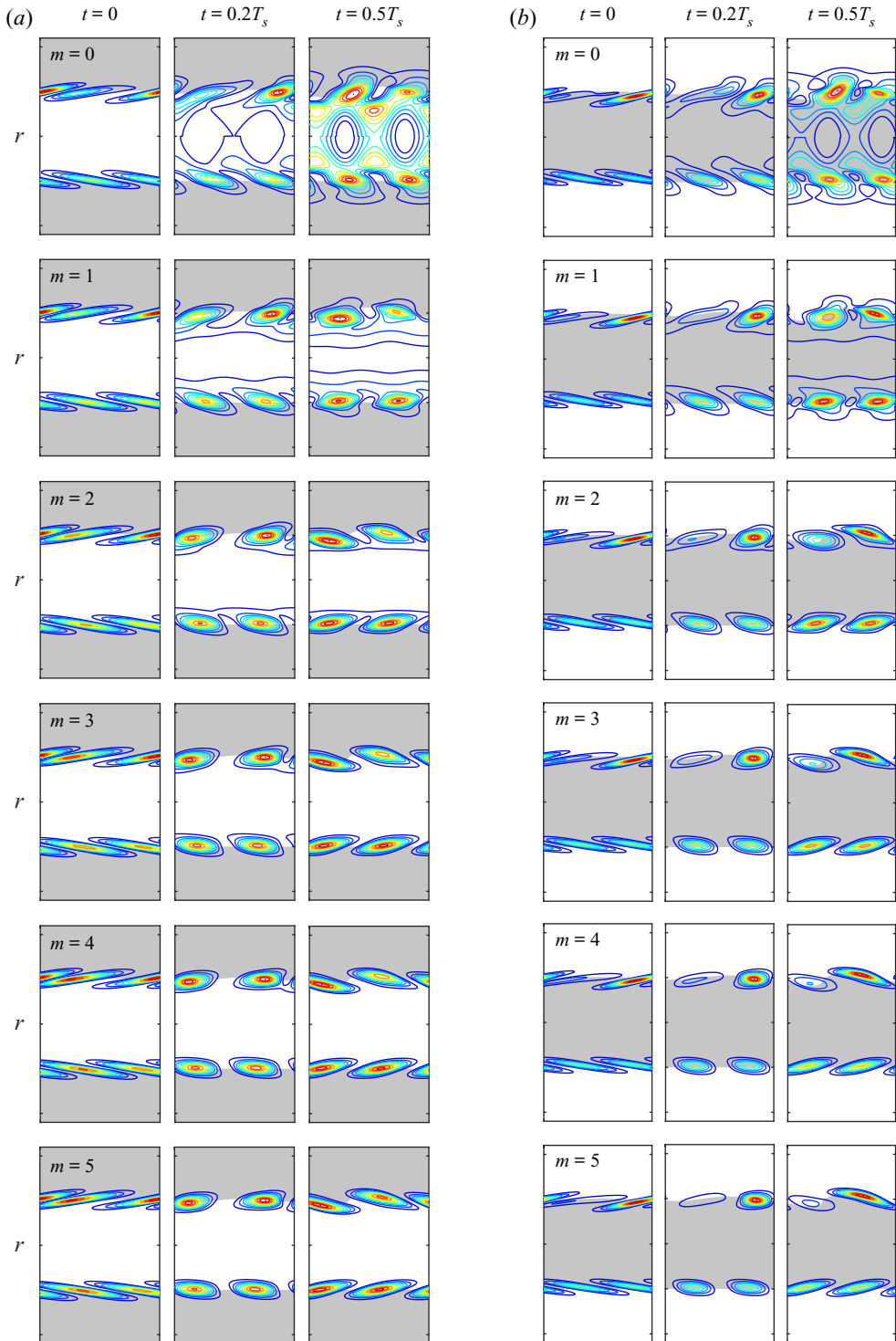


Figure 6. Early time evolution of the kinetic energy field  $E$  of optimal perturbations growing over a diffusing unperturbed parallel jet (lower half-plane) and a perturbed jet (upper half-plane), at (a)  $At = -0.25$  and (b)  $At = 0.25$ , for all the azimuthal wavenumbers considered in figure 5. The horizon time for the optimisation is  $T = T_s/2$ . The energy is normalised by the maximum value at each time and 10 equally spaced contour levels are used.



Optimal growth over a time-evolving VD jet at  $|At| = 0.25$

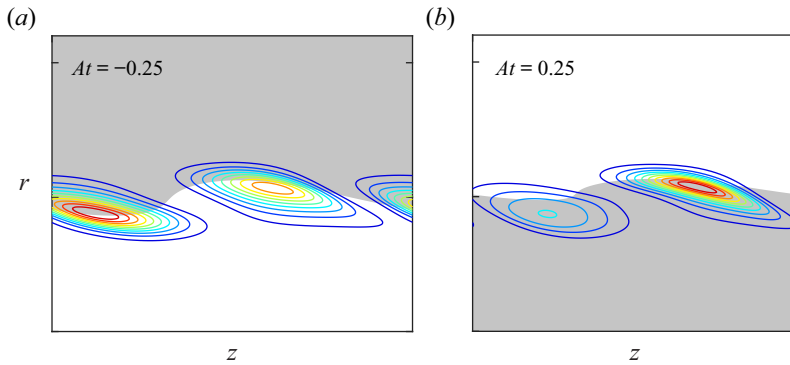


Figure 7. Close-up views taken from figure 6 for  $m = 3$  and  $T = T_s/2$ .

symmetric whereas the addition of a primary KH instability in the base flow induces an asymmetry between the two layers: that located in the region that will form the outer side of the braid is more energetic. The difference in the energy peak between the two layers is more pronounced for the heavy jet than for the light one. For later times at  $At = -0.25$ , the larger peak relocates from the outer side towards the inner side of the braid which hosts the main source of baroclinic vorticity production. This loss of symmetry reflects the one observed in the base flow. Despite that asymmetry, the optimal perturbations are not very sensitive to the presence of the KH wave in the time interval  $[0, T_s/2]$  because the energy gains are all overlapping and the spatial distribution of the kinetic energy is quite comparable for both the unperturbed and the perturbed jet, as evidenced in figure 6. The base flow mean shear leads to a gradual deformation of these layers before their complete reorientation along the direction of maximal stretching of the base flow. This is a result of the combined action of the Orr (1907) and lift-up (Ellingsen & Palm 1975) mechanisms which are responsible for the transient energy growth of these so-called ‘OL’ perturbations, as already observed in homogeneous jets (Nastro *et al.* 2020) and in plane shear layers (Arratia *et al.* 2013; Lopez-Zazueta *et al.* 2016). The intensification/attenuation of one or the other layer over time conforms to the evolution of the base flow mean shear, itself driven by the uneven baroclinic vorticity sources and sinks, as described in section § 2.2. As a consequence, the optimal perturbation evolution differs between the light and the heavy jet. At  $t = T_s/2$ , the most energetic layer is located in the inner side of the braid in the light jet whereas it is located in the outer side for the heavy jet (see also the close-up views in figure 7 for the optimal perturbation with  $m = 3$ ). Nevertheless, this uneven distribution of energy between the two layers is balanced because the energy gain remains comparable to that obtained in the homogeneous case. Interestingly, this asymmetry is emphasised with increasing azimuthal wavenumber  $m$  in the heavy jet and decreased in the light one.

The initial growth of these ‘OL’ perturbations ruled by the combination of the two shear-driven transient mechanisms is generic of shear flows. The amplification of the radial velocity  $u_r$  by the Orr mechanism can strengthen the streamwise rolls involved in the production of longitudinal velocity streaks at play in the lift-up mechanism (Farrell & Ioannou 1993). Simultaneously, the intensification of the axial velocity  $u_z$ , fed by the lift-up mechanism, enhances the azimuthal vorticity and, as a consequence, affects the circulation whose conservation substantiates the Orr mechanism according to the Kelvin theorem.

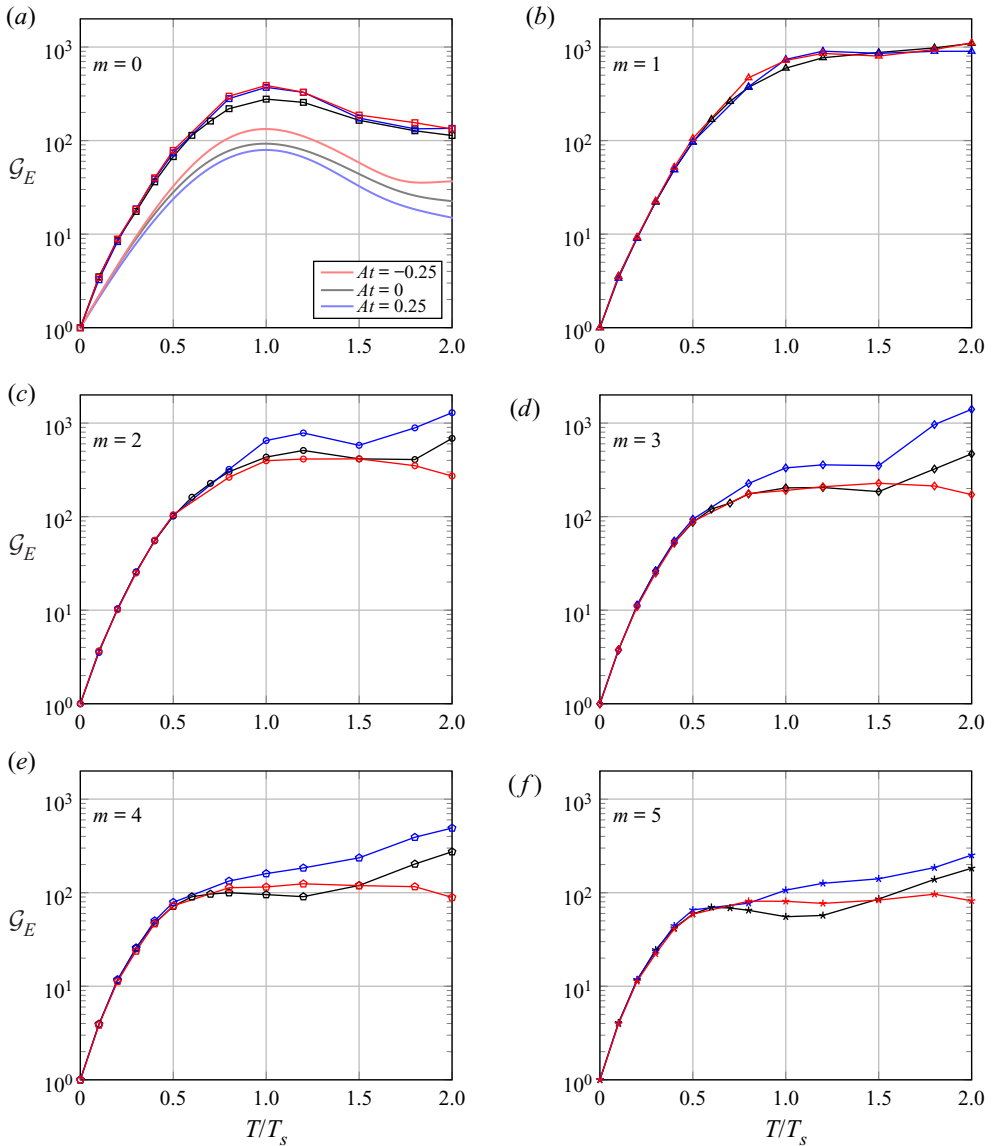


Figure 8. Optimal energy gain  $\mathcal{G}_E$  as a function of the time ratio  $T/T_s$  for  $At = -0.25$  (red),  $At = 0$  (black) and  $At = 0.25$  (blue), and for the same six azimuthal wavenumbers considered in figure 5. The thick continuous lines in the figure for the axisymmetric perturbation ( $m = 0$ ), correspond to the temporal evolution of the energy gain of the specific primary KH modes.

### 3.2. Second period $[T_s/2, 2T_s]$

We now consider the temporal evolution of the optimal perturbations in the period  $[T_s/2, 2T_s]$  during which the axisymmetric shear layer progressively rolls up into a nonlinear KH vortex ring. Figure 8 shows the optimal energy gain  $\mathcal{G}_E$  as a function of the normalised horizon time  $T/T_s$ , for azimuthal wavenumbers  $m$  up to five.

The optimal energy gains of disturbances growing over a homogeneous vortex ring, as obtained by Nastro *et al.* (2020), have been added for comparison. For  $At = -0.25$  the helical mode is the global optimal similar to the homogeneous case ( $At = 0$ ). For the heavy

jet ( $At = 0.25$ ), the helical perturbation is the global optimal up to  $T \approx 1.8T_s$ , after which the  $m = 2$  and  $m = 3$  modes present larger energy gains. The paths of energy growth of both the axisymmetric and helical perturbations do not show significant sensitivity to the Atwood number. The energy gain of the axisymmetric mode decreases after the KH saturation time, whereas the energy of the helical mode continues to grow slowly after  $T_s$ . The picture is quite different for modes with larger azimuthal wavenumbers. For  $m \geq 2$ , the disturbances growing over a heavy jet experience a substantial increase of their energy gains after the KH saturation time (especially for  $m = 3$ ) on a similar trend as the post-saturation growth observed in the homogeneous case. As their amplification before saturation is more efficient than for their homogeneous counterparts there is an offset between these two cases after  $T_s$ . However, in the light jet case, the energy gains of the perturbations are saturating if not decreasing for  $T > T_s$ . As a result, the optimal perturbations for  $At = -0.25$  present smaller energy gains for  $T > 1.5T_s$  than those of the perturbations growing on the homogeneous jet.

We now focus on the spatial distribution of the kinetic energy  $E$  of the optimal perturbations during the time interval  $[T_s, 2T_s]$  as displayed in [figure 9](#). The upper and lower half-planes correspond to the heavy and light jet configurations, respectively. The axisymmetric optimal perturbation for both  $At = -0.25$  and  $At = 0.25$  entails a linear transient growth relying on the 2D Orr mechanism, not exploited by the primary mode. This Orr-driven disturbance saturates due to the absence of any three-dimensional relay mechanism for a secondary energy growth. At this quite low Reynolds number, the optimal growth of the helical mode  $m = 1$  is found to be particularly unaffected by the modifications of the base flow field by density effects nor by the contribution of the linearised baroclinic torque. For larger azimuthal wavenumbers, the optimal perturbations in the heavy jet experience the combined development of E-type and H-type instabilities starting with a predominance of the elliptical mode at  $m = 1$  and evolving towards a preponderance of the hyperbolic one at  $m = 5$ . This change in regions of energy growth with increasing  $m$  is similar to what has been observed in the homogeneous case (Nastro *et al.* 2020). In the light jet, if the helical perturbation stands as an E-type instability, the structure of the perturbations at larger azimuthal wavenumbers differs from that observed in the homogeneous and heavy cases. Shortly after the KH saturation time  $T_s$ , we note a progressive concentration of the energy growth in a region located between the vortex core and the braid (see [figure 9](#) for  $m \geq 2$  at  $t = 5T_s/4$ ) which corresponds precisely to the base flow region hosting the largest strain intensity, as evidenced in § 2.2 (see [figure 4](#)).

The structure of the optimal perturbation with  $m = 4$  for  $At = -0.25$  is illustrated in [figure 10](#). In particular, we consider the spatial distribution of the three velocity components of the optimal perturbation at  $t = 1.2T_s$ , i.e. the time for which the light jet exhibits the relative maximum of the strain rate field. The axial velocity  $u_z$  is shown in the meridian plane whereas the radial  $u_r$  and azimuthal  $u_\theta$  velocity components are represented in the crosswise plane corresponding to the maximal value of the perturbation kinetic energy identified in [figure 9](#) and tagged as section K–K in [figure 10](#). The axial velocity is mainly concentrated in this region between the vortex core and the outer side of the braid where the base flow strain field is maximum (see [figure 4](#)). In the corresponding crosswise plane, periodic radial ejections/injections are observed and the azimuthal velocity is in quadrature with the radial velocity. This spatial distribution of perturbation velocity components in the K–K plane thus complies with the standard pattern of strained longitudinal vortices. [Figure 10\(d,e\)](#) displays the axial vorticity  $\omega_z$  in two distinct crosswise planes: a first lying in the braid in line with the hyperbolic stagnation point (section H–H) and the second in the vortex core in line with the elliptical stagnation

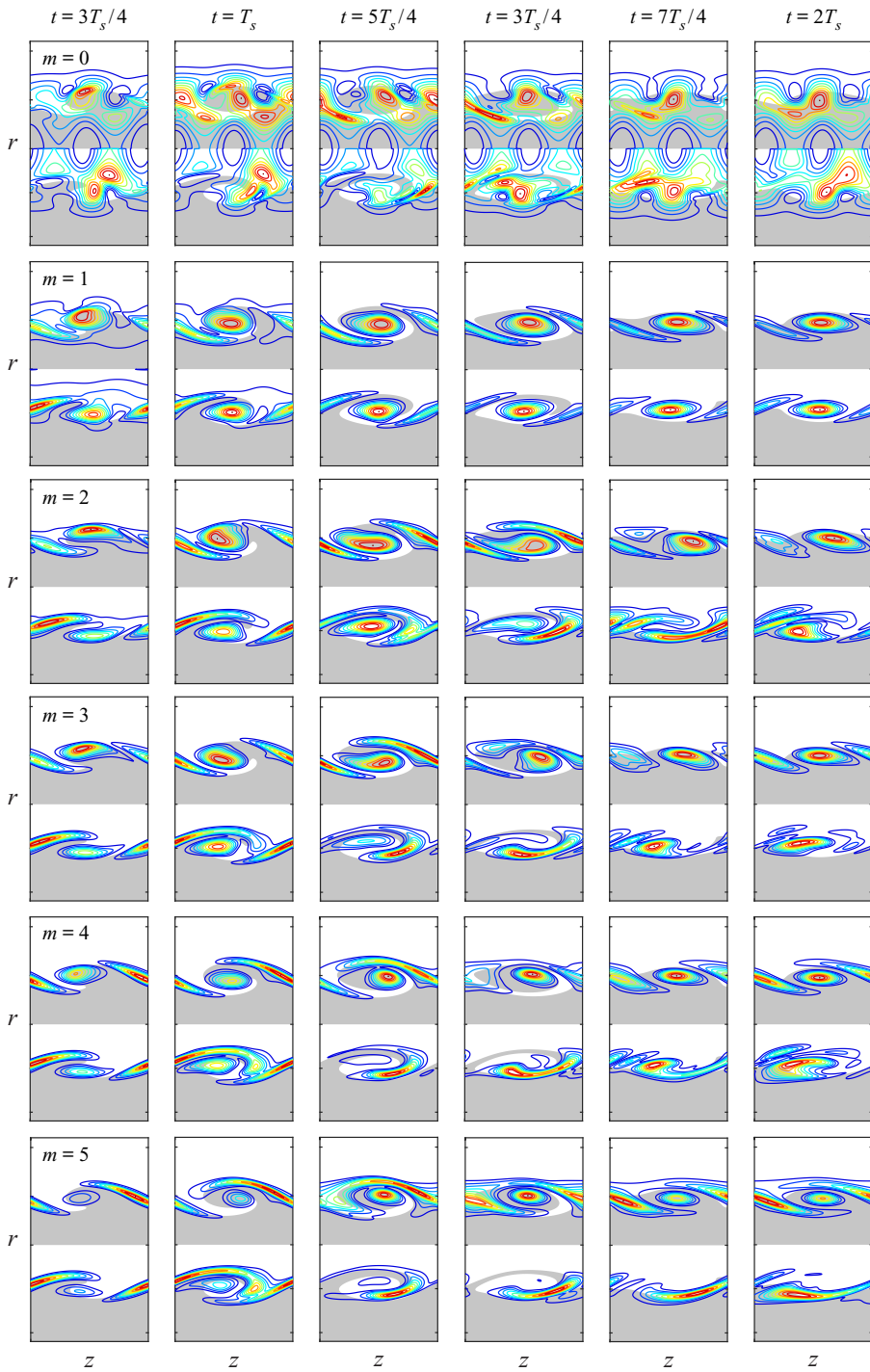


Figure 9. Temporal evolution of the kinetic energy field  $E$  of optimal perturbations from  $t = 3T_s/4$  to  $t = 2T_s$  for various azimuthal wavenumbers with  $At = 0.25$  (upper half-plane) and  $At = -0.25$  (lower half-plane). The optimisation time is  $T = 3T_s/2$ . The energy is normalised by the maximum value at each time for a given Atwood number and 10 equally spaced contour levels are used.

Optimal growth over a time-evolving VD jet at  $|At| = 0.25$

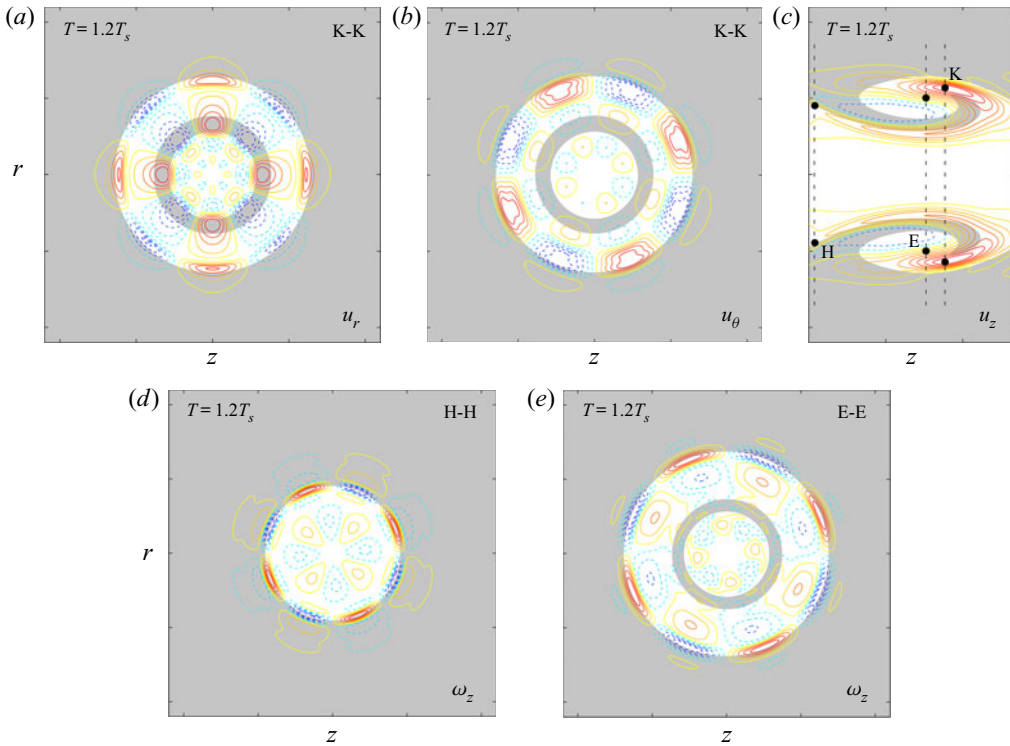


Figure 10. (a) Radial, (b) azimuthal and (c) axial velocity components and (d,e) axial vorticity of the optimal perturbation characterised by  $m = 4$  at  $t = T = 1.2T_s$  and  $At = -0.25$ . Points K, E and H indicate the location of the peak value of the perturbation energy, the elliptical and hyperbolic stagnation points, respectively. The radial and azimuthal velocity components are displayed in the crosswise plane K–K, whereas the axial velocity in the meridian plane. The axial vorticity  $\omega_z$  is represented in two crosswise planes: (d) plane H–H and (e) plane E–E. Contour levels are normalised by the local maximal absolute value, solid (respectively, dashed) contours correspond to positive (respectively, negative) values.

point (section E–E). In both cross-sections, four pairs of counter-rotating streamwise vortices concentrated along the mean outer isopycnal line are visible. They span the entire longitudinal extent of the jet and they induce the radial velocity field observed in the plane K–K. This mechanism of energy growth conforms to the mechanism of side-jet generation based on vortex induction advocated by Monkewitz & Pfizenmaier (1991) and, later, by Brancher *et al.* (1994). Our results thus plead in favour of the standard scenario, at least for a moderate negative Atwood number. In addition, the key ingredient of the distinct mechanism proposed by Lopez-Zazueta *et al.* (2016), i.e. the convergence/divergence towards the braid saddle point of longitudinal velocity streaks of opposite sign, is not retrieved as seen from figure 10(c), at least for this value of the Reynolds number.

### 3.3. Influence of the Reynolds number

In this section, we discuss the effect of the Reynolds number  $Re$  on the optimal perturbations. Figure 11 displays the temporal evolution of the energy gain  $\mathcal{G}_E$  for disturbances optimised for  $T = 3T_s/2$  at  $Re = 10\,000$  compared with those obtained at  $Re = 1000$ , for the same azimuthal wavenumbers. Owing to the corresponding diminution of the viscous dissipation, the increase in Reynolds number results in higher energy

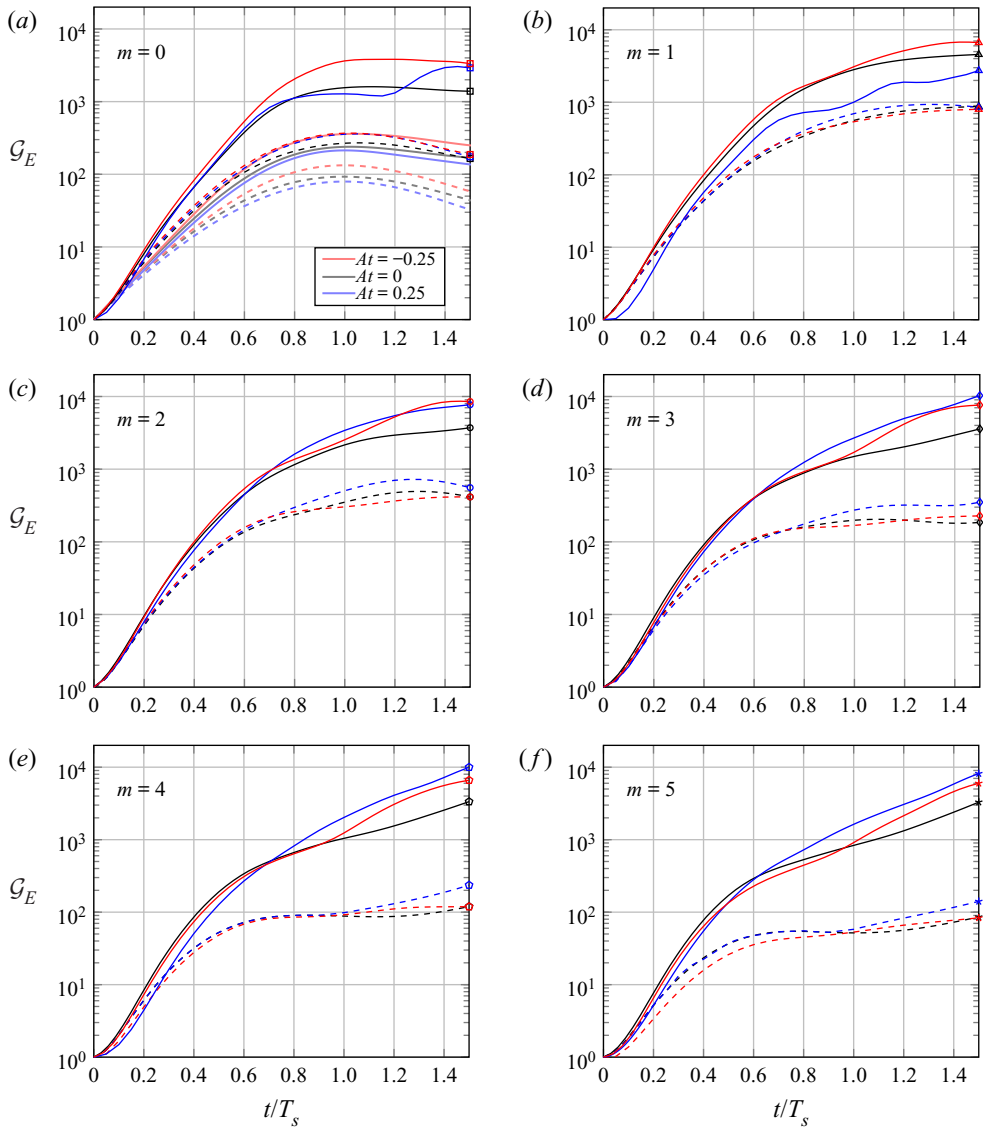


Figure 11. Temporal evolution of the energy gain  $\mathcal{G}_E$  of optimal perturbations at  $Re = 10000$  (solid lines) and  $Re = 1000$  (dashed lines) growing over a perturbed jet with  $At = -0.25$  (red),  $At = 0$  (black),  $At = 0.25$  (blue) and for six azimuthal wavenumbers  $m \in [0; 5]$ . The thick lines in the figure for  $m = 0$  represent the temporal evolution of the energy gain of the corresponding primary KH modes. The symbols are located at the horizon time of each energy curve.

gains but the extra growth is larger for variable-density situations compared with the homogeneous one, except for  $m = 1$  where the homogeneous perturbation shows an energy gain larger than that corresponding to the heavy jet case. For  $m \geq 2$ , this extra energy growth benefits more to the optimal perturbations of the light jet and yields a different hierarchy between the perturbations. At  $Re = 10000$  the optimal energy gain for  $At = -0.25$  is comparable to that for  $At = 0.25$  whereas it is lower at  $Re = 1000$ . The largest energy gain is attributed to the double-helix disturbance for the light jet and to the  $m = 3$  mode for the heavy jet, at least for  $t$  up to  $T = 1.5T_s$ . However, the strong similarity

Optimal growth over a time-evolving VD jet at  $|At| = 0.25$

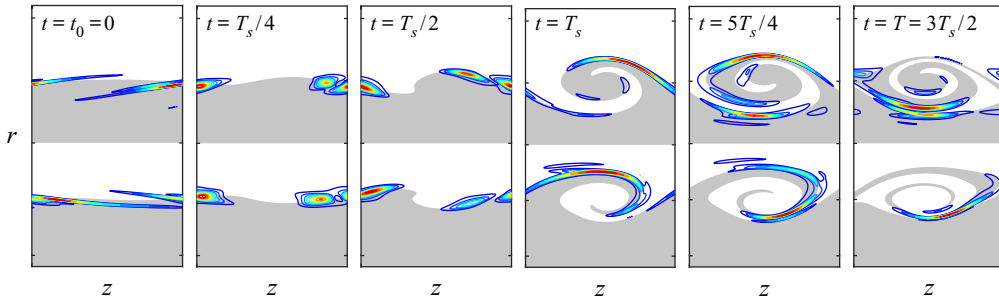


Figure 12. Temporal evolution of the kinetic energy field  $E$  of the optimal perturbation with  $m = 4$  and  $T = 3T_s/2$  growing over the heavy one (upper half-plane) and the light jet (lower half-plane). Same conventions as in figure 9.

between the amplification curves for  $m \geq 2$  at a given  $At$  is symptomatic of a loss of scale selectivity of the underlying base flow. As evidenced experimentally by Liepmann & Gharib (1992) and retrieved by the stability analysis of Nastro *et al.* (2020) in the homogeneous case, increasing the Reynolds number hampers selection of the azimuthal periodicity of secondary instabilities.

Figure 12 presents the time evolution of the kinetic energy field  $E$  from the injection time to  $T = 3T_s/2$  for the optimal  $m = 4$  perturbation developing on the heavy jet (upper half-plane) and on the light jet (lower half-plane). The optimal disturbance exhibits the same structure than that observed at  $Re = 1000$  but the two layers are much thinner as expected. The evolution during the first phase in the time interval  $[t_0, T_s/2]$  reflects the shear-driven growth due to the Orr and lift-up mechanisms. However, as soon as  $t = T_s/2$ , when the disturbance is aligned with the maximal stretching direction of the base flow, the localisation of the energy maximum starts to move towards the side of the braid which benefits from the baroclinic vorticity production (see figure 3). The subsequent evolution shows a strong correlation of the localisation of the kinetic energy of the perturbation with the regions of the base flow where the baroclinic vorticity production is active, at least up to saturation time. At the horizon time  $T = 3T_s/2$ , the production and base flow advection of the energy results in an optimal response essentially located at the outer periphery of the vortex core for the light jet case and at the inner periphery of the billow for the heavy jet.

For the light jet case, looking at the contribution of each velocity component to the evolution of the perturbation energy gain in figure 13(a), it can be seen that the energy growth is mainly due to the increase of the axial velocity  $u_z$ . Figure 13(b) shows also that the growth of the perturbation enstrophy is clearly driven by the azimuthal vorticity  $\omega_\theta$  which is almost two orders of magnitude larger than the other vorticity components at the horizon time. The corresponding budgets for the energy and enstrophy growth rates rate are given in figure 13(c,d) according to (2.19) and (2.22). Although the initial growth of both quantities is driven by the base flow shear conversion owing to the Orr and lift-up mechanisms, the growth in the second phase for  $t \approx 7T_s/10$  results from a combination of the base flow strain conversion, measured by  $\sigma_{E_2}$  for the energy and  $\sigma_{Z_{4+5}}$  for the enstrophy, and the action of the baroclinic torque, i.e. the terms  $\sigma_{E_{4+5}}$  for the energy and  $\sigma_{Z_7}$  for the enstrophy. As stated by (2.26), the azimuthal component  $b_\theta$  of the linearised baroclinic torque results from the sum of two contributions:

$$b_\theta = \underbrace{a_z \frac{1}{R} \frac{\partial R}{\partial r} - a_r \frac{1}{R} \frac{\partial R}{\partial z}}_{b_{\theta_1}} + \underbrace{A_z \frac{\partial}{\partial r} \left( \frac{\rho}{R} \right) - A_r \frac{\partial}{\partial z} \left( \frac{\rho}{R} \right)}_{b_{\theta_2}}. \quad (3.1)$$

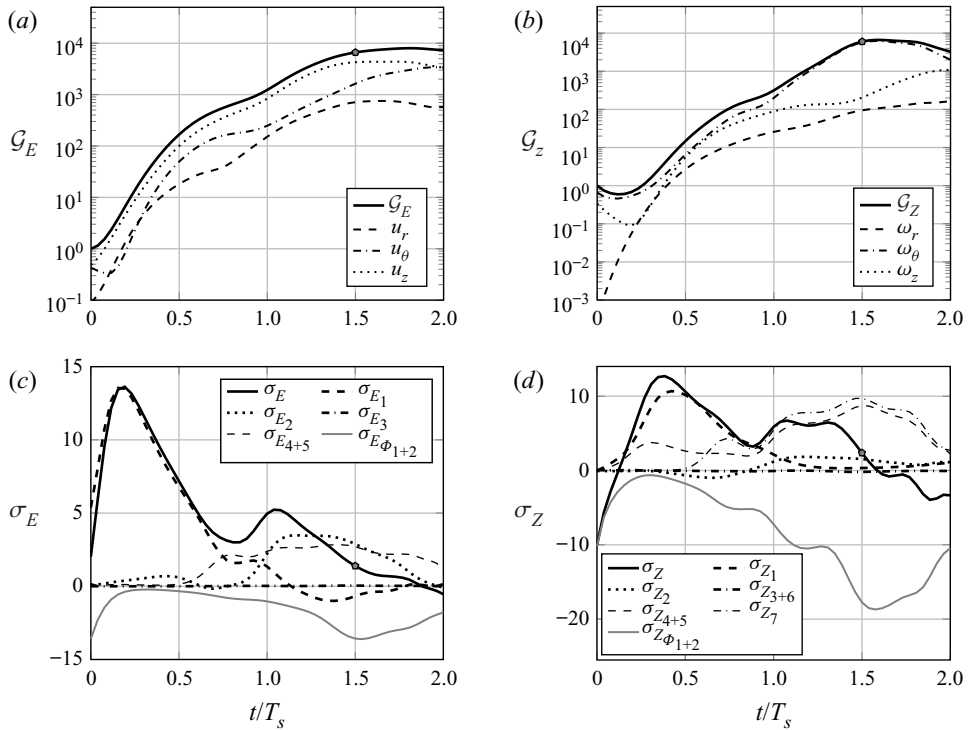


Figure 13. Temporal evolution of (a) the kinetic energy growth rate  $\sigma_E$  and (b) the entrophy growth rate  $\sigma_Z$  for the optimal perturbation at  $m = 4$  and  $At = -0.25$  with their corresponding budgets (c) and (d), according to (2.19) and (2.28), respectively. The horizon time is  $T = 3T_s/2$  (as indicated by the symbol on each curve).

As observed also in the plane mixing layer by Lopez-Zazueta *et al.* (2016, figure 13), although the first term  $b_{\theta_1}$  is predominant in the early development of perturbations, the second phase proceeds with baroclinic production from the term  $b_{\theta_2}$  (not shown) associated with large-amplitude density perturbation. Its evolution from  $t = 3T_s/4$  to  $t = 3T_s/2$  is illustrated on the first row of figure 14 for the  $m = 4$  optimal perturbation. At  $t = 3T_s/4$ , it consists of two thin layers of density perturbation of opposite sign located along the braid. Combined with the local base flow acceleration, it yields the specific structure of azimuthal baroclinic torque supported by the sketch of vectors at  $t = 3T_s/4$  shown in the second row of figure 14. This spatial distribution of  $b_\theta$  in the form of two layers of opposite sign along the braid on either side of the saddle point yields a similar azimuthal vorticity distribution. The structuration of the perturbation azimuthal vorticity driven by the component  $b_{\theta_2}$  of the linearised baroclinic torque continues up to the horizon time as indicated by the strong similarity between the two fields. According to Biot–Savart induction, these vorticity layers yield elongated patches of longitudinal velocity at their interface as seen in the last row of figure 14. At  $T = 3T_s/2$ , the disturbance axial velocity field consists of two parallel elongated layers of opposite sign located at the outer periphery of the vortex ring where the perturbation kinetic energy is concentrated, see figure 12. This mechanism of secondary energy growth is the same as that identified by Lopez-Zazueta *et al.* (2016) in the variable-density mixing layer but the structuration of the optimal perturbation at the horizon is here quite different.

As for the heavy jet case, figure 15 shows similarly the energy (a) and entrophy (b) gains up to  $t = 2T_s$  along with the relative contribution of each velocity/vorticity component



Optimal growth over a time-evolving VD jet at  $|At| = 0.25$

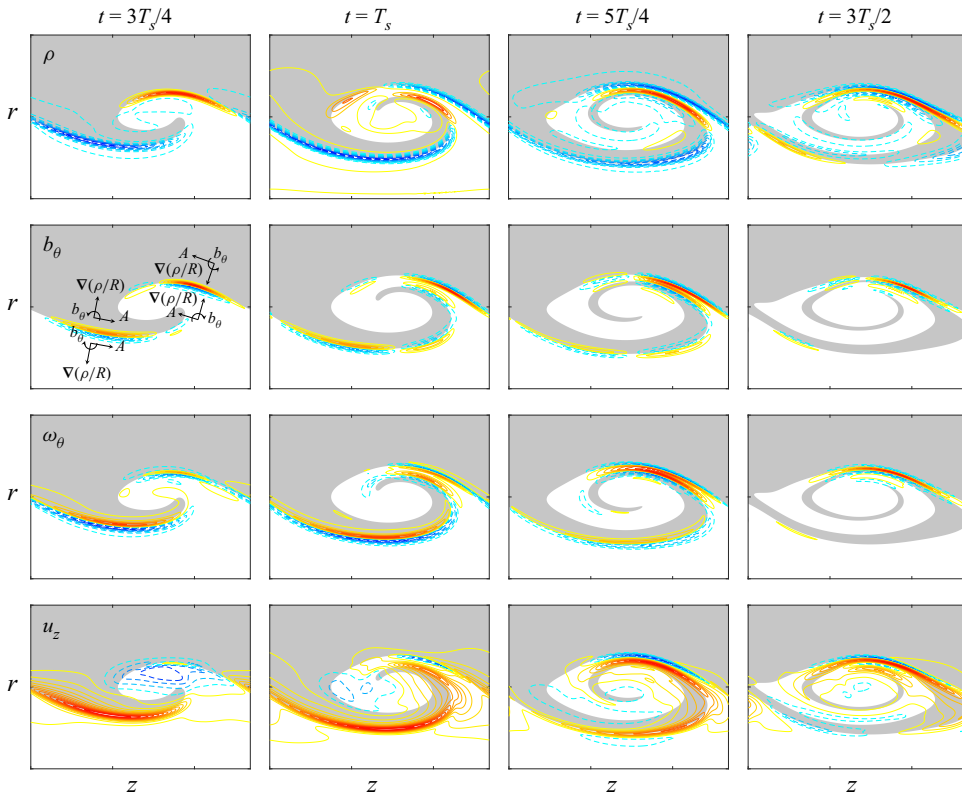


Figure 14. Temporal evolution of density  $\rho$ , azimuthal component of the baroclinic torque  $b_\theta$ , azimuthal vorticity  $\omega_\theta$  and axial velocity  $u_z$  of the optimal  $m = 4$  perturbation during the time interval  $[3T_s/4, 3T_s/2]$ . The perturbation is optimised for  $T = 3T_s/2$  with  $At = -0.25$ .

for the same parameters,  $m = 4$  and  $T = 1.5T_s$ . The corresponding contributions to the temporal evolution of the energy and enstrophy growth rates according to (2.19) and (2.22) are shown in figures 15(c) and 15(d). We denote a strong anisotropy in the energy and enstrophy growths which are born by the axial velocity and the azimuthal vorticity, respectively. Beyond the first phase of universal shear-driven growth ending around  $t \approx 7T_s/10$ , the energy increase is due to the baroclinic torque  $\sigma_{E_{4+5}}$  combined alternatively with the base flow strain term  $\sigma_{E_2}$  and the base flow shear conversion term  $\sigma_{E_1}$ . As in the light jet case, post-saturation enstrophy growth relies on baroclinic vorticity production  $\sigma_{Z_7}$  and the base flow strain conversion  $\sigma_{Z_{4+5}}$ . As illustrated in figure 16, the associated physical mechanism is the same as for the optimal perturbation in the light jet. The structure of the perturbation azimuthal vorticity is driven by the component  $b_{\theta_2}$  of the linearised baroclinic torque which results from the combination of the local two-dimensional base flow acceleration field and the perturbation density, as illustrated by the sketch of vectors at  $t = T_s$  in the second row of figure 14. The distribution of  $\omega_\theta$  leads to two elongated axial velocity layers which are localised at the horizon time at inner periphery of the KH vortex core, where the perturbation kinetic energy is concentrated in figure 12.

This optimal perturbation leading to an intense shear layer on the braid outer side for the light jet and on the inner one for the heavy jet contrasts with that observed at smaller Reynolds number. Therefore, this instability could be involved in the side-jet generation

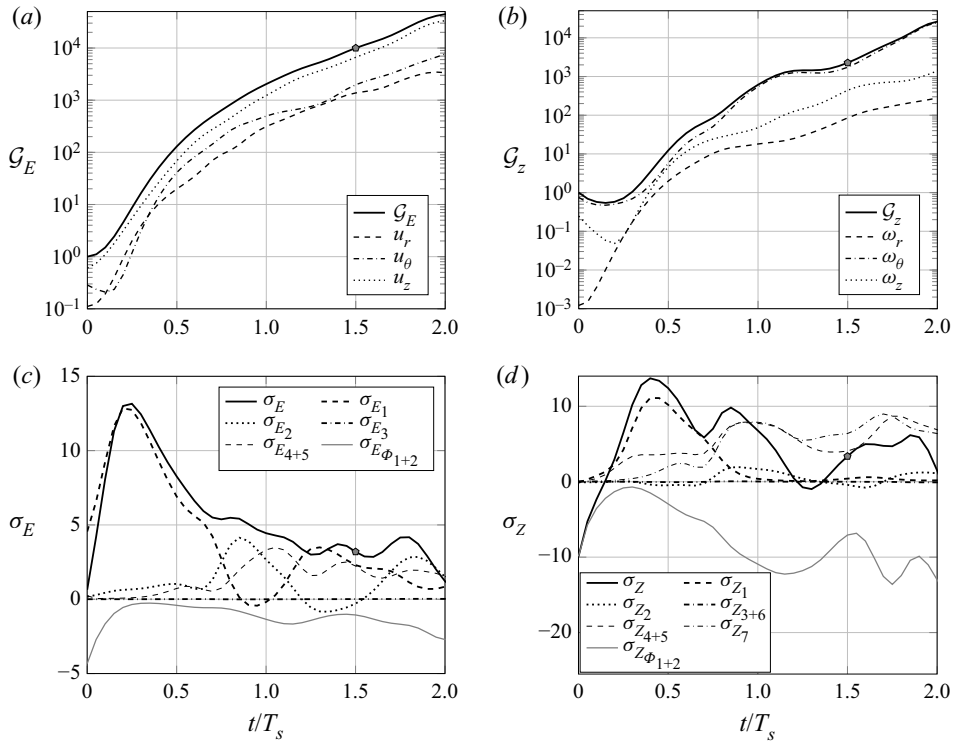


Figure 15. Temporal evolution of (a) the kinetic energy growth rate  $\sigma_E$  and (b) the entrophy growth rate  $\sigma_z$  for the optimal perturbation with  $m = 4$  and  $At = 0.25$  with their corresponding budgets (c) and (d), according to (2.19) and (2.28), respectively. The horizon time is  $T = 3T_s/2$  (as specified by the symbol on each curve).

and the difference in the location of the perturbation between the light and heavy jets could be related to the observation of side jets in the light case only.

For both the light and heavy jet, the increase in Reynolds number yields higher energy gains which are associated with the same physical mechanism first identified by Lopez-Zazueta *et al.* (2016) in the variable-density mixing layer. Here, the optimal response takes the form of two layers of axial velocity both localised on the inner side of the KH vortex core in the case of the heavy jet and on the outer side for the light jet configuration. The density variation thus turns the paradigm of saddle-centred counter-rotating streamwise vortices into a quite different optimal response. However, it is slightly different from the longitudinal velocity streaks of opposite sign along the braid on either side of the hyperbolic saddle point observed in the plane variable-density mixing layer. It stands as a third candidate path to three-dimensionalisation for variable-density shear flows but its connection with side-jet generation remains unclear.

### 3.4. Influence of the injection time and fractal KH breakups

In § 3.1 we found that the Atwood number  $At$  has no influence on the early evolution of optimal perturbations. We now delay the instant of perturbation beyond the first universal phase to elucidate secondary growth mechanisms over a well developed but unperturbed KH roll-up. An injection time of  $t_0 = 7T_s/10$  is thus selected in order to leave out the short-time energy growth driven by both the Orr and lift-up mechanisms. Figure 17 displays the time evolution of the energy gain  $\mathcal{G}_E$  for the corresponding optimal

Optimal growth over a time-evolving VD jet at  $|At| = 0.25$

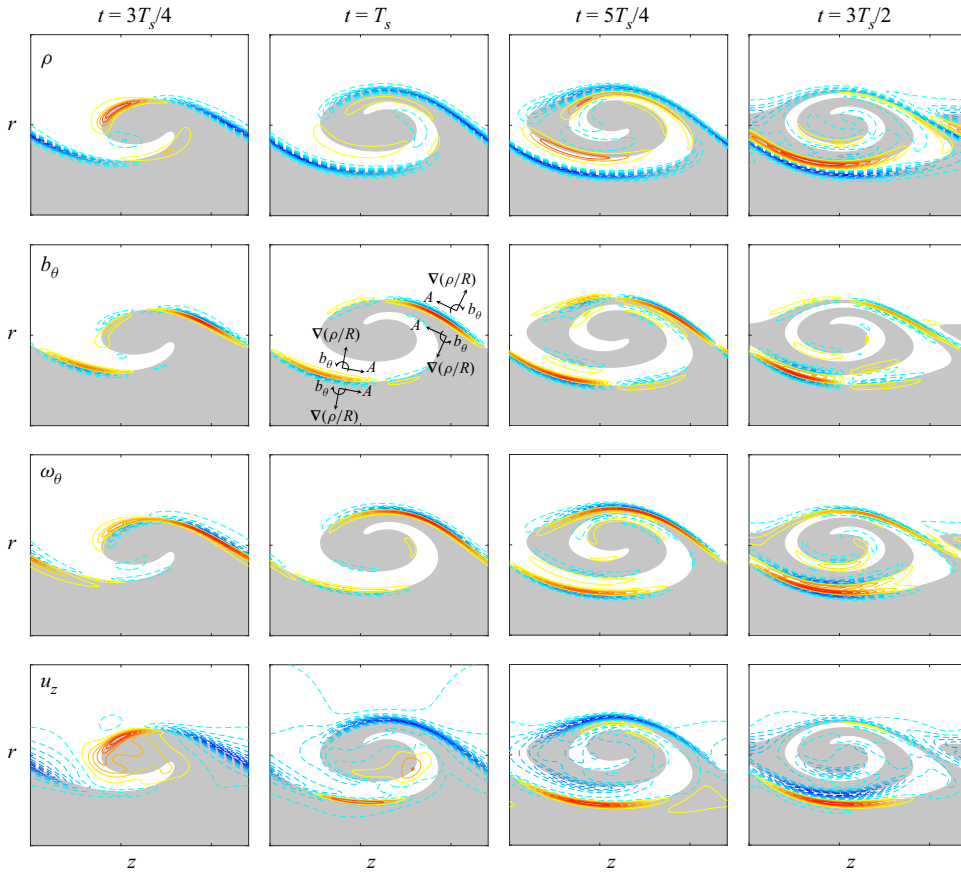


Figure 16. Temporal evolution of density  $\rho$ , azimuthal component of the baroclinic torque  $b_\theta$ , azimuthal vorticity  $\omega_\theta$  and axial velocity  $u_z$  of the optimal  $m = 4$  perturbation at  $At = 0.25$  during the time interval  $[3T_s/4, 3T_s/2]$ . The horizon time is  $T = 3T_s/2$ .

perturbations for all the azimuthal wavenumbers considered here. The horizon time is  $T = 2T_s$  and two Reynolds numbers are considered, i.e.  $Re = 1000$  and  $Re = 10000$ . For  $Re = 1000$ , the energy gain reached at the horizon time is, as expected, much lower than when growth benefits from the powerful transient growth resulting from shear-driven OL mechanisms in the initial stage (before  $7T_s/10$ ). This observation holds whatever the Atwood number in the present range, presumably because mass diffusion at unitary Schmidt number and vorticity diffusion in the base flow both prevent the secondary growth that is strikingly steep for a higher Reynolds number. Although homogeneous optimal perturbations for  $Re = 10000$  only weakly benefit from higher shear and lower dissipation, the variable-density optimal growth with postponed injection exhibits intense monotonic energy growth, with energy gains as high as around  $10^6$  at horizon time. We have verified (not shown) that the delayed energy growth of secondary perturbations at  $Re = 1000$  resorts to standard E-type and H-type secondary instabilities. For the base flow rolling-up into a high-Reynolds-number variable-density vortex ring, the supplementary growth of energy is very likely to be associated with a different physical mechanism. Figure 18 shows the contributions to the temporal evolution of the energy and enstrophy growth rates according to (2.19) and (2.28) for the axisymmetric optimal perturbations

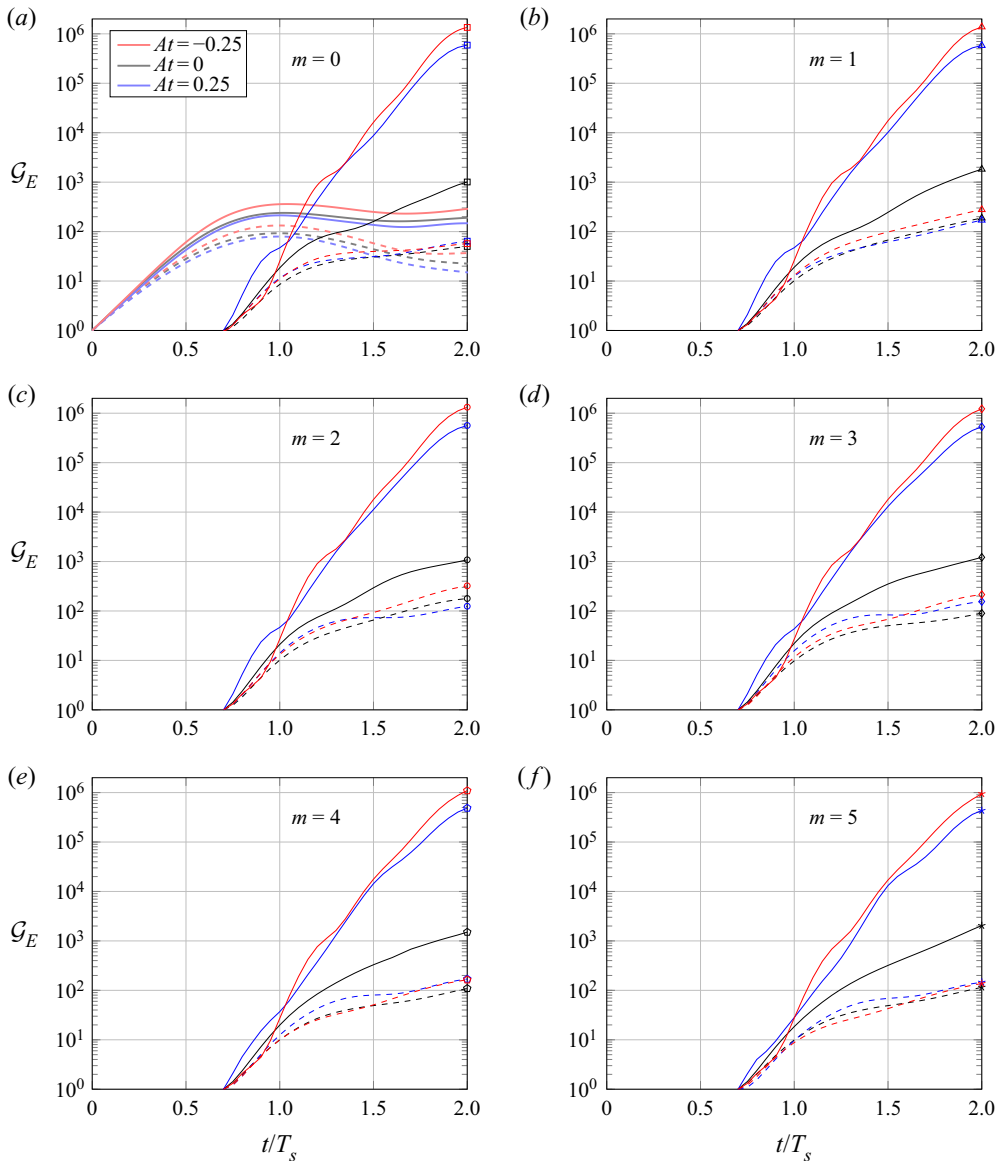


Figure 17. Temporal evolution of the energy gain  $\mathcal{G}_E$  of optimal perturbations injected at  $t_0 = 7T_s/10$  for  $Re = 10000$  (solid lines) and  $Re = 1000$  (dashed lines) growing over a perturbed jet at  $At = -0.25$  (red),  $At = 0$  (black) and  $At = 0.25$  (blue) and for the same six azimuthal wavenumbers considered in figure 16. The thick lines in the figure for  $m = 0$  represent the temporal evolution of the energy gain of the corresponding primary KH modes. The symbols are located at the horizon time of each energy curve.

( $m = 0$ ) optimised for  $T = 2T_s$ . The initial growth is seen to be driven by the base flow shear conversion identified by term  $\sigma_{E_1}$  but it is shortly replaced by the term  $\sigma_{E_{4+5}}$  in (2.19) and  $\sigma_{Z_7}$  in (2.28) which correspond to the baroclinic vorticity production. In agreement with the energy gains plotted in figure 17, the energy and enstrophy growth rates of the disturbances developing on the light jet are slightly higher than those of the perturbations for the heavy jet. Figure 19 presents the temporal evolution of the fields of density and azimuthal vorticity of the axisymmetric optimal perturbation for both the light

Optimal growth over a time-evolving VD jet at  $|At| = 0.25$

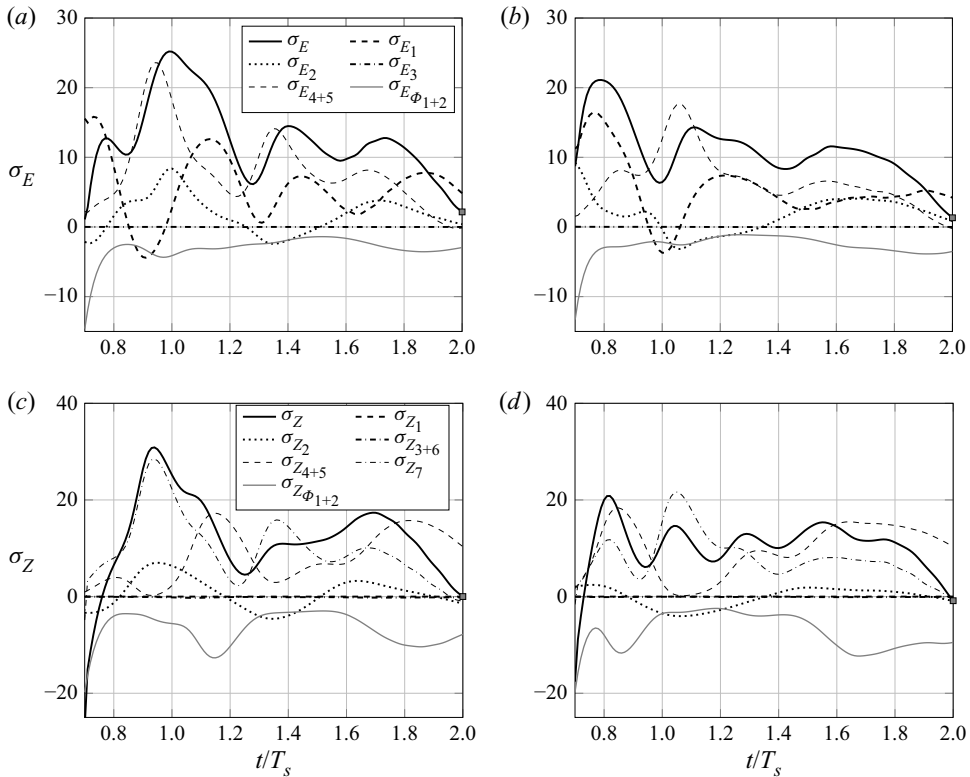


Figure 18. Temporal evolution of (a,b) the kinetic energy growth rate  $\sigma_E$  and (c,d) the enstrophy growth rate  $\sigma_Z$  with their different contributions according to (2.19) and (2.28) for the axisymmetric optimal perturbation growing over a KH vortex ring with (a,c)  $At = -0.25$  and (b,d)  $At = 0.25$ . As evidenced by the symbol on each curve, the horizon time is  $T = 2T_s$ .

and the heavy jet. The optimal excitation consists of small elongated spanwise vorticity and density patches of alternate sign located along the outer side of the braid for the heavy jet and the inner side of the braid for the light jet. It corresponds to the region where the base flow baroclinic torque represents a source of azimuthal vorticity  $\Omega_\theta$  (see figure 1). This structure is characteristic of the secondary KH instability first observed by Reinaud *et al.* (2000). The subsequent time evolution shows that the disturbance is convected towards the core of the KH vortex ring. The same spatial distribution is observed for all non-zero azimuthal wavenumbers. As demonstrated by Reinaud *et al.* (2000), the baroclinic secondary KH instability is triggered when inertial baroclinic vorticity production supersedes the stabilising effect of stretching along the vorticity braid. Because baroclinic vorticity production benefits from the increase in Reynolds number for fixed Atwood and Schmidt numbers, the secondary KH instability is expected to emerge at some flow-dependant Reynolds number. We deduce that the onset of secondary baroclinic KH instability occurs between  $Re = 1000$  and  $Re = 10000$  in the present case. Lopez-Zazueta *et al.* (2016) retrieved the secondary KH mode in the variable-density mixing layer for a Reynolds number  $Re = 1000$ , based on the shear layer width. This is consistent with the present value of  $Re = 10000$  based on the jet radius, provided that the aspect ratio of the present jet is  $\alpha = 10$ . It is demonstrated in Lopez-Zazueta *et al.* (2016) that the secondary KH instability developing over a planar mixing-layer

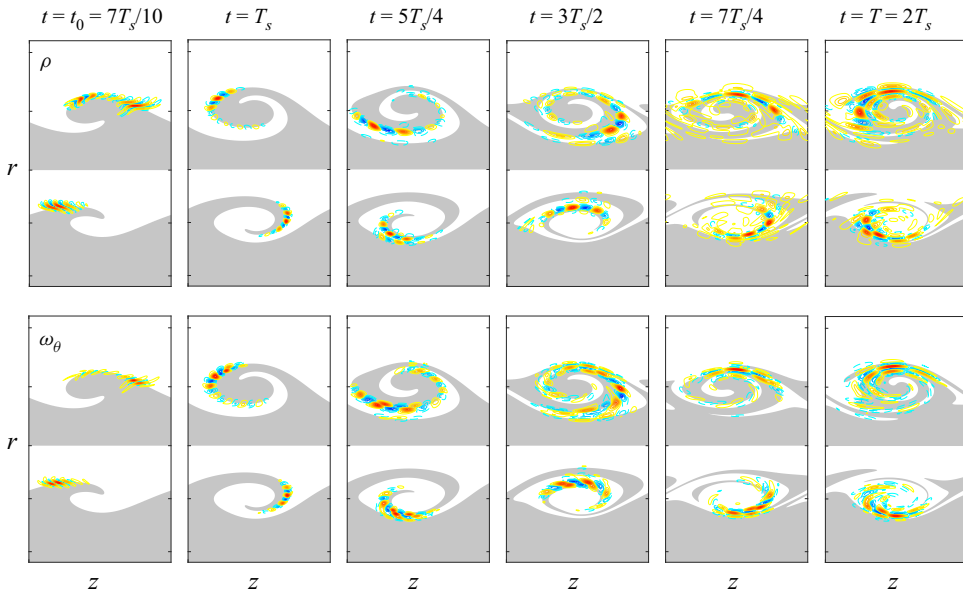


Figure 19. Linear evolution of the axisymmetric optimal perturbation ( $m = 0$ ) for  $Re = 10\,000$  with  $At = 0.25$  (upper half-plane) and  $At = -0.25$  (lower half-plane) from  $t = t_0 = 7T_s/10$  to  $t = T = 2T_s$  in terms of (upper row) density  $\rho$  and (lower row) azimuthal vorticity  $\omega_\theta$ . The quantities are normalised by the corresponding maximum value at each time for a given Atwood number.

is a two-dimensional mechanism for which oblique versions with non-zero spanwise wavenumbers exhibit weaker energy growth than the two-dimensional one, i.e. that with a streamwise wave vector perpendicular to base-flow KH roll-ups. We stress that in the present situation, the growth that builds up on the same mechanism, is only slightly weaker for non-zero azimuthal wavenumbers. As seen from [figure 17](#), the response to optimal perturbations with oblique wave vectors is following almost exactly the same route in terms of energy growth over a large range of azimuthal wavenumbers suggesting a loss of azimuthal selectivity. The proposed temporal approach with delayed injection gives an estimate of the potential of energy growth and of the associated receptivity to ambient perturbations downstream the nozzle of a spatially developing jet. However, because real-world perturbations are not controlled two-dimensional ones, we conjecture that baroclinic secondary KH instabilities are more likely to occur in real jets than in plane mixing layers.

We choose to illustrate this path for secondary growth even beyond the linear stage by means of a nonlinear simulation stemming from a base flow perturbed with the axisymmetric optimal perturbation. This results into the development of a secondary KH instability as shown in [figure 20](#) for both the light and the heavy KH vortex ring. In the light jet, the inner side of the braid experiences undulations yielding the development of secondary KH breakups within the primary vortex ring. In the heavy jet, a similar evolution happens on the outer side of the braid (see [figures 20a](#) and [20b](#)). At later times we also observe the emergence of a curvature-driven Rayleigh–Taylor instability, similar to the one observed by [Joly \*et al.\* \(2005\)](#). As illustrated by [figures 20\(e\)](#) and [20\(f\)](#), it occurs at the interface between the jet and the surrounding fluid due to centripetal acceleration induced by the curvature of fluid particle trajectories. It is evidenced by the formation of opposite-sign secondary vortices (as opposed to like-signed ones for the secondary

Optimal growth over a time-evolving VD jet at  $|At| = 0.25$

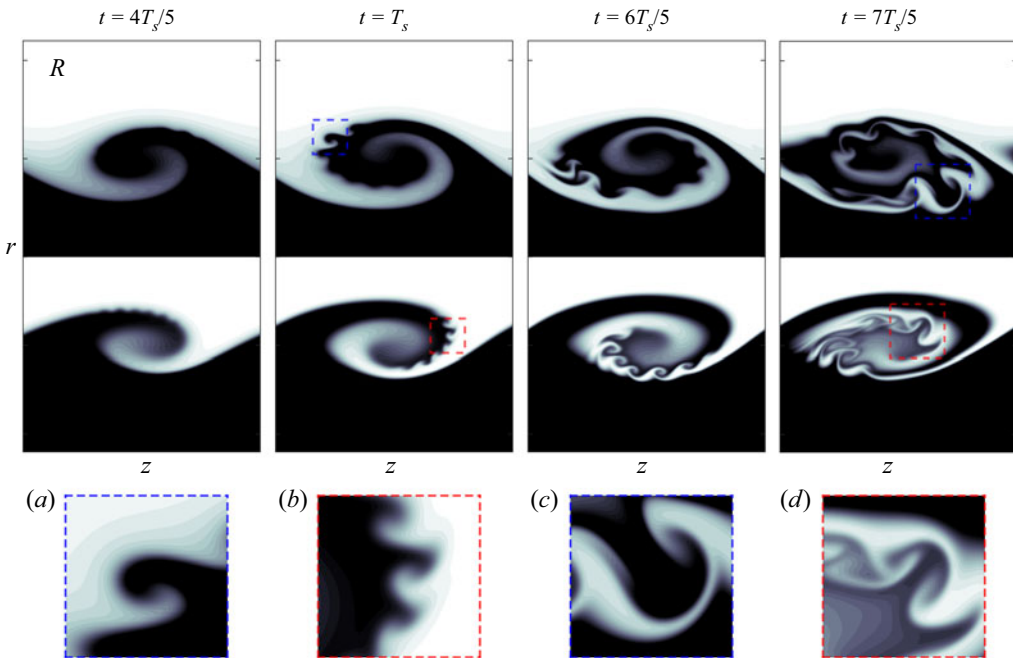


Figure 20. Temporal development of the secondary KH instabilities for  $Re = 10\,000$  with  $At = 0.25$  (upper half-plane) and  $At = -0.25$  (lower half-plane) for  $t = 4T_s/5, T_s, 6T_s/5, 7T_s/5$ : (a,b) close-up insets on the KH vortex ring at  $t = T_s$  and (c,d) relative to  $t = 7T_s/5$ , as evidenced by the square-shaped regions showing where the zoom is located. All pictures display the flow density field  $R$ .

KH instability, see figures 20c and 20d) yielding mushroom-shaped density contours, as evidenced by figures 20(g) and 20(h). The late stages of evolution show a fast increase of the length of isopycnic lines due to the stretching between secondary vortices, both promoting mixing between the two fluids.

Though thriving in the nonlinear regime, the oblique secondary KH instability cannot be related to side ejections in any way. Primary or secondary KH billows are organised as rows of corotating vortices along shear layers, yielding a strong deformation of the hyperbolic regions. As secondary structures developing in the present context over a primary KH vortex ring, they promote local mixing but they cannot induce radial velocities. In contrast, the onset of oblique secondary KH instability is likely to be the reason of the disappearance of side jets at large Reynolds numbers and of the particularly short route to turbulence observed in the light jets experiments of Fontane (2005).

#### 4. Conclusions

In this paper, we have investigated the potential for transient growth of secondary perturbations developing over a time-dependent variable-density round jet subject to the primary KH instability. This base flow is calculated via a nonlinear direct numerical simulation initialised with hyperbolic tangent velocity and density profiles (Michalke 1971; Fontane 2005; Nichols *et al.* 2007), perturbed by the most amplified axisymmetric KH mode. We adopt a direct-adjoint approach to determine the optimal perturbation maximising the gain of kinetic energy over a specific time interval  $[t_0, T]$ . The aspect ratio  $\alpha$  between the jet radius and the shear layer momentum thickness has been fixed to  $\alpha = 10$ . We use two values for both the Atwood number,  $At = -0.25$  and  $At = 0.25$  for a light

and heavy jet, respectively, and the Reynolds number, i.e.  $Re = 1000$  and  $Re = 10\,000$ . The Schmidt number is set to  $Sc = 1$  and represents a good approximation for the binary mixing of gases.

The initially parallel base flow evolves towards a KH vortex ring which experiences baroclinic vorticity production. The contributions of the baroclinic torque stands as an asymmetric dipole centred on the braid saddle point. These variable-density sources and sinks enhance the existing loss of central symmetry of the vorticity field, already induced by the cylindrical geometry in the homogeneous case (Nastro *et al.* 2020). This redistribution of vorticity comes along with an intensification of the strain field in a region between the vortex core and the outer side of the braid for the light jet and the inner side for the heavy one, shortly after the KH saturation.

Up to half the KH saturation time, the optimal perturbations grow according to a universal path whatever the Atwood number  $At$  for both the perturbed and unperturbed jet. They exhibit the classical ‘OL’ form characterised by two elongated layers which are gradually deformed by the base flow mean shear and reoriented along the direction of maximal stretching. Their transient energy growth relies on a combination of the Orr (1907) and lift-up (Ellingsen & Palm 1975) mechanisms. At  $T = T_s/2$ , in the light jet, the perturbation energy concentrates in a layer located on the inner side of the braid, whereas in the heavy jet, it grows preferentially in a layer located on the outer side of the braid.

Beyond  $T_s/2$ , the optimal energy gains become sensitive to the density variations because the amplification curves branch off to different paths, except for the axisymmetric ( $m = 0$ ) and helical ( $m = 1$ ) disturbances. For  $At = -0.25$ , the helical mode stands as the global optimal, similar to the homogeneous case. For the heavy jet, the  $m = 1$  mode displays the largest values of  $\mathcal{G}_E$  until  $T \approx 1.5T_s$ , after which the  $m = 2$  and  $m = 3$  modes become more amplified. In the heavy jet, the structure of the optimal perturbations are similar to those obtained in the homogeneous jet (Nastro *et al.* 2020): a combination of a core-centred E-type and a braid-centred H-type instabilities whose distribution evolves from a predominance of the E-type to the H-type when the azimuthal wavenumber is increased. In the light jet, the perturbation kinetic energy peaks in the region between the KH vortex core and the outer side of the braid, precisely where the base flow exhibits a local intensification of the strain rate. In the crosswise plane corresponding to the maximal value of the perturbation kinetic energy, the perturbation exhibits periodic radial ejections/injections induced by counter-rotating streamwise vortices spanning the entire longitudinal extent of the jet. This structure of the perturbation is similar to that observed in homogeneous jets and supports the mechanism of side ejections proposed by Monkewitz & Pfizenmaier (1991) and, later, by Brancher *et al.* (1994).

Increasing the Reynolds number by one order of magnitude results in a more efficient transient energy growth for all perturbations. In the second period, high anisotropy in energy and enstrophy growths is observed with a sustained amplification of the axial velocity and the azimuthal vorticity with respect to the other components. The perturbation density field is at the origin of this energy growth through its contribution to the azimuthal baroclinic torque which drives the linear dynamics, as in the variable-density mixing layer (Lopez-Zazueta *et al.* 2016). However, the resulting streamwise streaks of alternate signs along the braid identified by Lopez-Zazueta *et al.* (2016) are replaced here by a shear layer localised on the outer side of the KH vortex ring for the light jet and on the inner side for the heavy jet case.

At  $Re = 10\,000$ , delaying the disturbance injection past the time of nonlinear roll-up of the variable-density KH vortex ring, triggers the emergence of the secondary KH instability, originally identified by Reinaud *et al.* (2000) in plane mixing layers. Energy



gains three order of magnitude larger than those observed in the homogeneous case are evidenced at all azimuthal wavenumbers  $m$ . Considering the very large growth rate associated with this mechanism, we conjecture that this instability might participate in the rapid transition observed in high-Reynolds-number variable-density jet flows.

The causal relationship between absolute instability and side jets, which suffers from some exceptions in the parameter space, does not exhaust all questions about the how of side ejections: underlying mechanism and local structure of the flow, fixed streamwise position of side ejections and their survival to interruptions by vortex rings passing by the ejection section, variation of the ejection angle in the  $(S, Re)$ -plane, preferred azimuthal periodicity. The transition to absolute instability below a critical  $S$  brings in the period-to-period synchronisation of an oscillator, which is exactly realised in the time-evolving approach. Although not suitable for addressing the already solved question of convective-absolute transition, the present framework provides answers to the effect of variable density on the vortex ring combined with the secondary baroclinic torque production in the disturbance field. We propose to extend this global stability analysis to higher Atwood number cases in order to emphasise the influence of baroclinic vorticity sources, both in the base flow and the perturbation vorticity fields. We think this is highly relevant to the three-dimensionalisation process of highly-contrasted variable-density jets and we plan to pay particular attention to round jets with a density ratio representative of the hydrogen–air couple, i.e.  $S = 0.07$  and  $At = -0.87$ , because they stand as prototype flows for fuel injectors in combustion chambers of future turbojet engines. With mixing promotion in mind, an extension of this approach to the nonlinear regime with the introduction of specific seminorms adapted to the optimisation of mixing (Foures, Caulfield & Schmid 2014) would be of great interest.

**Funding.** This research is supported in part by the French Ministry of Defence through financial support of the DGA under Grant number 2016635 and in part by the Institut Supérieur de l’Aéronautique et de l’Espace (ISAE-SUPAERO). It has been performed using HPC resources from GENCI-IDRIS and GENCI-CINES on Jean Zay, Occigen (Grant number A0102A07178) and CALMIP on Olympe (Grant number 2021-p1425).

**Declaration of interests.** The authors report no conflict of interest.

**Author ORCIDs.**

-  Gabriele Nastro <https://orcid.org/0000-0002-7561-7502>;
-  Jérôme Fontane <https://orcid.org/0000-0003-2033-8677>;
-  Laurent Joly <https://orcid.org/0000-0002-0016-3104>.

**Appendix A. Strain tensor**

The strain rate tensor  $\mathbf{D}$  for the base flow takes the following form:

$$\mathbf{D} = \frac{1}{2}(\nabla \mathbf{U} + \nabla \mathbf{U}^T) = \begin{bmatrix} \frac{\partial U_r}{\partial r} & 0 & \frac{1}{2} \left( \frac{\partial U_z}{\partial r} + \frac{\partial U_r}{\partial z} \right) \\ 0 & \frac{U_r}{r} & 0 \\ \frac{1}{2} \left( \frac{\partial U_z}{\partial r} + \frac{\partial U_r}{\partial z} \right) & 0 & \frac{\partial U_z}{\partial z} \end{bmatrix}, \quad (\text{A1})$$

where the superscript  $T$  denotes the Hermitian transpose. Its deviatoric part is defined by  $\mathbf{D}_0 = \mathbf{D} - \frac{1}{3}(\nabla \cdot \mathbf{U})\mathbf{I}$  where  $\mathbf{I}$  is the identity tensor. In order to study the spatial distribution of  $\mathbf{D}_0$ , we consider its Euclidean norm  $\|\mathbf{D}_0\|_2 \equiv \text{tr}(\mathbf{D}_0^2)$ .

**Appendix B. Linear matrix operators**

The linear matrix operators of the direct (2.11) and adjoint (2.18) systems take the following form:

(1) the temporal operator

$$N_t = \begin{bmatrix} \frac{\partial \star}{\partial t} & 0 & 0 \\ 0 & \frac{\partial \star}{\partial t} & 0 \\ 0 & 0 & 0 \end{bmatrix}; \tag{B1}$$

(2) the direct operator of coupling between the base flow and the perturbation

$$N_c = \begin{bmatrix} U \cdot \nabla \star + \nabla U \cdot \star & -\frac{1}{R^2} \nabla P & \frac{1}{R} \nabla \star \\ \nabla R \cdot \star + R \nabla \cdot \star & U \cdot \nabla \star + (\nabla \cdot U) \star & 0 \\ \nabla \cdot \star & 0 & 0 \end{bmatrix}; \tag{B2}$$

(3) the direct diffusion operator

$$N_d = \begin{bmatrix} -\frac{1}{R} \left[ \Delta \star + \frac{1}{3} \nabla (\nabla \cdot \star) \right] & \frac{\star}{R^2} \left[ \Delta U + \frac{1}{3} \nabla (\nabla \cdot U) \right] & 0 \\ 0 & 0 & 0 \\ 0 & \frac{1}{Sc} \Delta \left( \frac{\star}{R} \right) & 0 \end{bmatrix}; \tag{B3}$$

(4) the adjoint operator of coupling between the base flow and the adjoint perturbation

$$N_c^\dagger = \begin{bmatrix} -U \cdot \nabla \star - (\nabla \cdot U) \star + \nabla U^T \cdot \star & -R \nabla \star & -\nabla \star \\ -\frac{1}{R^2} \nabla P \cdot \star & -U \cdot \nabla \star & 0 \\ \nabla \cdot \left( \frac{\star}{R} \right) & 0 & 0 \end{bmatrix}; \tag{B4}$$

(5) the adjoint diffusion operator

$$N_d^\dagger = \begin{bmatrix} -\Delta \left( \frac{\star}{R} \right) - \frac{1}{3} \nabla \left[ \nabla \cdot \left( \frac{\star}{R} \right) \right] & 0 & 0 \\ \frac{1}{R^2} \left[ \Delta U + \frac{1}{3} \nabla (\nabla \cdot U) \right] \cdot \star & 0 & \frac{1}{ScR} \Delta \star \\ 0 & 0 & 0 \end{bmatrix}. \tag{B5}$$

The symbol  $\star$  denotes either the components of the direct vector  $q$  or adjoint vector  $q^\dagger$ .

**Appendix C. The iterative optimisation algorithm**

The outline of the iterative optimisation algorithm used to determine the optimal perturbation is as follows.

- (1) A white noise perturbation  $\mathbf{q}^{(i)}(t_0)$  is chosen as an initial condition for the direct system (2.11). Its kinetic energy is given by

$$\|\mathbf{q}(t_0)\|_u = E_0, \tag{C1}$$

where the seminorm

$$\|\mathbf{q}\|_u = \|\mathbf{u}\| = [\mathbf{q} | \mathbf{W}^u \cdot \mathbf{q}] \tag{C2}$$

is associated with the inner product  $[\star | \star]$  defined by

$$[\mathbf{q}_1 | \mathbf{q}_2] = \int_0^{r_{max}} \int_0^{2\pi} \int_0^{L_z} \mathbf{q}_1^* \cdot \mathbf{q}_2 r \, dr \, d\theta \, dz + \text{c.c.}, \tag{C3}$$

where the exponent  $*$  stands for the complex conjugate and the matrix operator  $\mathbf{W}^u$  is defined by

$$\mathbf{W}^u = \begin{bmatrix} 1 & 0 & 0 \\ 0 & 0 & 0 \\ 0 & 0 & 0 \end{bmatrix}. \tag{C4}$$

If any value for the constant  $E_0$  is possible in practice, it was fixed here to  $E_0 = 1$  for all cases.

- (2) The direct system (2.11) is advanced in time from the injection time  $t_0$  up to the horizon time  $T$  with the linearised version of the pseudo-spectral method used for the simulation of the primary KH vortex ring.
- (3) The energy gain  $G_E^{(i)}$  of the direct perturbation is calculated as defined by (2.13). Then, if the kinetic energy criterion

$$\frac{G_E^{(i)} - G_E^{(i-1)}}{G_E^{(i-1)}} \leq \varepsilon \tag{C5}$$

is below a chosen threshold, here  $\varepsilon = 0.005$ , the iterative method has converged towards the optimal perturbation. Otherwise, we turn to the next step.

- (4) The final state of the perturbation  $\mathbf{q}(T)$  is used to compute the initial condition for the adjoint system (2.18) as follows:

$$\mathbf{W}^u \cdot \mathbf{q}^\dagger(T) = \mathbf{W}^u \cdot \mathbf{q}(T). \tag{C6}$$

- (5) The adjoint system (2.18) is integrated backward in time from  $T$  to  $t_0$  with the same numerical pseudo-spectral method used for the direct equations.
- (6) At the injection time  $t_0$ , the new initial condition  $\mathbf{q}^{(i+1)}(t_0)$  is obtained through the optimality condition

$$\Lambda_u \mathbf{W}^u \cdot \mathbf{q}(t_0) - \mathbf{q}^\dagger(t_0) = 0, \tag{C7}$$

where the Lagrange multiplier  $\Lambda_u$  is chosen so as to rescale the velocity field with respect to (C1). Then we go back to step 2 until the convergence is reached.

#### REFERENCES

- ARRATIA, C., CAULFIELD, C.P. & CHOMAZ, J.-M. 2013 Transient perturbation growth in time-dependent mixing layers. *J. Fluid Mech.* **717**, 90–133.
- BATCHELOR, G.K. & GILL, A.E. 1962 Analysis of the stability of axisymmetric jets. *J. Fluid Mech.* **14** (4), 529–551.
- BECKER, H.A. & MASSARO, T.A. 1968 Vortex evolution in a round jet. *J. Fluid Mech.* **31** (3), 435–448.

- BRANCHER, P., CHOMAZ, J.-M. & HUERRE, P. 1994 Direct numerical simulations of round jets: vortex induction and side jets. *Phys. Fluids* **6** (5), 1768–1774.
- COENEN, W., LESSHAFFT, L., GARNAUD, X. & SEVILLA, A. 2017 Global instability of low-density jets. *J. Fluid Mech.* **820**, 187–207.
- CORBETT, P. & BOTTARO, A. 2000 Optimal perturbations for boundary layers subject to stream-wise pressure gradient. *Phys. Fluids* **12** (1), 120–130.
- CORBETT, P. & BOTTARO, A. 2001 Optimal linear growth in swept boundary layers. *J. Fluid Mech.* **435**, 1–23.
- CRIGHTON, D.G. & GASTER, M. 1976 Stability of slowly diverging jet flow. *J. Fluid Mech.* **77** (2), 397–413.
- DIMOTAKIS, P.E. 1986 Two-dimensional shear-layer entrainment. *AIAA J.* **24** (11), 1791–1796.
- DRAZIN, P.G. & REID, W.H. 1981 *Hydrodynamic Stability*. Cambridge University Press.
- ELLINGSEN, T. & PALM, E. 1975 Stability of linear flow. *Phys. Fluids* **18** (4), 487–488.
- FARRELL, B.F. 1988 Optimal excitation of perturbations in viscous shear flow. *Phys. Fluids* **31** (8), 2093–2102.
- FARRELL, B.F. & IOANNOU, P.J. 1993 Perturbation growth in shear flow exhibits universality. *Phys. Fluids A* **5** (9), 2298–2300.
- FONTANE, J. 2005 Transition des écoulements cisailés libres à densité variable. PhD thesis, Institut National Polytechnique de Toulouse, France.
- FONTANE, J. & JOLY, L. 2008 The stability of the variable-density Kelvin–Helmholtz billow. *J. Fluid Mech.* **612**, 237–260.
- FONTANE, J., JOLY, L. & REINAUD, J.N. 2008 Fractal Kelvin–Helmholtz breakups. *Phys. Fluids* **20** (9), 091109.
- FOURES, D.P.G., CAULFIELD, C.P. & SCHMID, P.J. 2014 Optimal mixing in two-dimensional plane Poiseuille flow at finite Péclet number. *J. Fluid Mech.* **748**, 241–277.
- GARNAUD, X., LESSHAFFT, L., SCHMID, P.J. & HUERRE, P. 2013a Modal and transient dynamics of jet flows. *Phys. Fluids* **25** (4), 044103.
- GARNAUD, X., LESSHAFFT, L., SCHMID, P.J. & HUERRE, P. 2013b The preferred mode of incompressible jets: linear frequency response analysis. *J. Fluid Mech.* **716**, 189–202.
- GUNZBURGER, M. 2002 *Perspectives in Flow Control and Optimization*. Society for Industrial and Applied Mathematics.
- HALLBERG, M.P. & STRYKOWSKI, P.J. 2006 On the universality of global modes in low-density axisymmetric jets. *J. Fluid Mech.* **569**, 493–507.
- JENDOUBI, S. & STRYKOWSKI, P.J. 1994 Absolute and convective instability of axisymmetric jets with external flow. *Phys. Fluids* **6** (9), 3000–3009.
- JIMENEZ-GONZALEZ, J.I. & BRANCHER, P. 2017 Transient energy growth of optimal streaks in parallel round jets. *Phys. Fluids* **29** (11), 114101.
- JIMENEZ-GONZALEZ, J.I., BRANCHER, P. & MARTINEZ-BAZAN, C. 2015 Modal and non-modal evolution of perturbations for parallel round jets. *Phys. Fluids* **27** (4), 044105.
- JOLY, L., FONTANE, J. & CHASSAING, P. 2005 The Rayleigh–Taylor instability of two-dimensional high-density vortices. *J. Fluid Mech.* **537**, 415–431.
- JOLY, L. & REINAUD, J.N. 2007 The merger of two-dimensional radially stratified high-Froude-number vortices. *J. Fluid Mech.* **582**, 133–151.
- JOSEPH, D.D. 1990 Fluid dynamics of two miscible liquids with diffusion and gradient stresses. *Eur. J. Mech. (B/Fluids)* **9** (6), 565–596.
- KLAASSEN, G.P. & PELTIER, W.R. 1991 The influence of stratification on secondary instability in free shear layers. *J. Fluid Mech.* **227**, 71–106.
- KYLE, D.M. & SREENIVASAN, K.R. 1993 The instability and breakdown of a round variable density jet. *J. Fluid Mech.* **249**, 619–664.
- LANDHAL, M.T. 1975 Wave breakdown and turbulence. *SIAM J. Appl. Maths* **28** (4), 735–756.
- LANDHAL, M.T. 1980 A note on an algebraic instability of inviscid parallel shear flows. *J. Fluid Mech.* **98** (2), 243–251.
- LESSEN, M.P. & SINGH, P.J. 1973 The stability of axisymmetric free shear layers. *J. Fluid Mech.* **60** (3), 433–457.
- LESSHAFFT, L. & HUERRE, P. 2007 Linear impulse response in hot round jets. *Phys. Fluids* **19** (2), 024102.
- LESSHAFFT, L., HUERRE, P. & SAGAUT, P. 2007 Frequency selection in globally unstable round jets. *Phys. Fluids* **19** (5), 054108.
- LESSHAFFT, L., HUERRE, P., SAGAUT, P. & TERRACOL, M. 2006 Nonlinear global modes in hot jets. *J. Fluid Mech.* **554**, 393–409.
- LIEPMANN, D. & GHARIB, M. 1992 The role of streamwise vorticity in the near-field entrainment of round jets. *J. Fluid Mech.* **245**, 643–668.

*Optimal growth over a time-evolving VD jet at  $|At| = 0.25$*

- LOPEZ-ZAZUETA, A., FONTANE, J. & JOLY, L. 2016 Optimal perturbations in time-dependent variable-density Kelvin–Helmholtz billows. *J. Fluid Mech.* **803**, 466–501.
- LUCHINI, P. & BOTTARO, A. 1998 Görtler vortices: a backward-in-time approach to the receptivity problem. *J. Fluid Mech.* **363**, 1–23.
- LUCHINI, P. & BOTTARO, A. 2001 Linear stability and receptivity analyses of the stokes layer produced by an impulsively started plate. *Phys. Fluids* **13** (6), 1668–1678.
- MICHALKE, A. 1971 Instabilität eines kompressiblen runden freistrahls unter berücksichtigung des einflusses des strahlgrenzschichtdicke. *Z. Flugwiss.* **8–9**, 319–328.
- MICHALKE, A. 1984 Survey on jet instability theory. *Prog. Aerosp. Sci.* **21**, 159–199.
- MONKEWITZ, P.A. & BECHERT, D.W. 1988 Self-excited oscillations and mixing in a hot jet. *Phys. Fluids* **31** (9), 2386–2386.
- MONKEWITZ, P.A., BECHERT, D.W., BARSIKOW, B. & LEHMANN, B. 1990 Self-excited oscillations and mixing in a heated round jet. *J. Fluid Mech.* **213**, 611–639.
- MONKEWITZ, P.A., LEHMANN, B., BARSIKOW, B. & BECHERT, D.W. 1989 The spreading of self-excited hot jets by side jets. *Phys. Fluids* **1** (3), 446–448.
- MONKEWITZ, P.A. & PFIZENMAIER, E. 1991 Mixing by side jets in strongly forced and self-excited round jets. *Phys. Fluids* **3** (5), 1356–1361.
- MORRIS, P.J. 1976 The spatial viscous instability of axisymmetric jets. *J. Fluid Mech.* **77** (3), 511–529.
- MOSER, R.D. & ROGERS, M.M. 1993 The three-dimensional evolution of a plane mixing layer: pairing and transition to turbulence. *J. Fluid Mech.* **247**, 275–320.
- NASTRO, G. 2020 Stabilité non-modale des jets ronds inhomogènes. PhD thesis, Université de Toulouse, Institut Supérieur de l’Aéronautique et de l’Espace.
- NASTRO, G., FONTANE, J. & JOLY, L. 2020 Optimal perturbations in viscous round jets subject to Kelvin–Helmholtz instability. *J. Fluid Mech.* **900**, A13.
- NICHOLS, J.W., SCHMID, P.J. & RILEY, J.J. 2007 Self-sustained oscillations in variable-density round jets. *J. Fluid Mech.* **582**, 341–376.
- ORR, W.M.F. 1907 The stability or instability of the steady motions of a perfect liquid and of a viscous liquid. Part I: A perfect liquid. Part II: A viscous liquid. *Proc. R. Irish Acad. A: Math. Phys. Sci.* **27**, 9–138.
- ORTIZ, S. & CHOMAZ, J.-M. 2011 Transient growth of secondary instabilities in parallel wakes: anti lift-up mechanism and hyperbolic instability. *Phys. Fluids* **23** (11), 114106.
- PLASCHKO, P. 1979 Helical instabilities of slowly divergent jets. *J. Fluid Mech.* **92**, 209–215.
- RAYLEIGH, J.W.S. 1892 *Scientific Papers*, vol. 3, Cambridge Library Collection – Mathematics. Cambridge University Press.
- REINAUD, J.M., JOLY, L. & CHASSAING, P. 2000 The baroclinic secondary instability of the two-dimensional shear layer. *Phys. Fluids* **12** (10), 2489–2505.
- ROGERS, M.M. & MOSER, R.D. 1993 Spanwise scale selection in plane mixing layers. *J. Fluid Mech.* **247**, 321–337.
- SANDOVAL, D.L. 1995 The dynamics of variable-density turbulence. PhD thesis, University of Washington, USA.
- SCHMID, P.J. 2007 Nonmodal stability theory. *Annu. Rev. Fluid Mech.* **39** (1), 129–162.